Pacific Northwest
NATIONAL LABORATORY

PNNL-33210

Corrosion of U233-Doped Uranium Oxide using Microfluidics Methods

Spent Fuel and Waste Form Science and Technology FY2022 Report

August 2022

Jennifer Yao
Shalini Tripathi
Eugene S. Ilton
Bruce K. McNamara
Nabajit Lahiri
Matthew J. O'Hara
Shawn L. Riechers
Edgar C. Buck

U.S. DEPARTMENT OF ENERGY

Prepared for the U.S. Department of Energy
under Contract DE-AC05-76RL01830

PACIFIC NORTHWEST NATIONAL LABORATORY
operated by
BATTELLE
for the
UNITED STATES DEPARTMENT OF ENERGY
under Contract DE-AC05-76RL01830

Printed in the United States of America

Available to DOE and DOE contractors from the
Office of Scientific and Technical Information,
P.O. Box 62, Oak Ridge, TN 37831-0062;
ph: (865) 576-8401
fax: (865) 576-5728
email: reports@adonis.osti.gov

Available to the public from the National Technical Information Service
5301 Shawnee Rd., Alexandria, VA 22312
ph: (800) 553-NTIS (6847)
email: orders@ntis.gov <https://www.ntis.gov/about>
Online ordering: http://www.ntis.gov

PNNL-33210

Corrosion of U233-Doped Uranium Oxide using Microfluidics Methods

Spent Fuel and Waste Form Science and Technology FY2022 Report

August 2022

Jennifer Yao
Shalini Tripathi
Eugene S. Ilton
Bruce K. McNamara
Nabajit Lahiri
Matthew J. O’Hara
Shawn L. Riechers
Edgar C. Buck

Prepared for
the U.S. Department of Energy
under Contract DE-AC05-76RL01830

Pacific Northwest National Laboratory
Richland, Washington 99354

Abstract

The aim of work this year has been to investigate the role of alpha (α)-radiation and hydrogen (H_2) on the corrosion of uranium oxide (UO_2) using a microfluidic device. The microfluidic device, termed the Particle-Attached Microfluidic Electrochemical Cell, (PAMEC), enables monitoring of the UO_2 electrochemical corrosion potential (E_{corr}) under different environments, including de-aerated conditions and in the presence of dissolved H_2. The Si_3N_4 window allows us to study morphological and chemical changes under an electron microscope. We have previously demonstrated that the PAMEC matches the results from bulk electrochemical tests with UO_2 [1]. We used the high specific activity uranium (U) isotope, ^{233}U, ($t_{1/2}$ = 160,000 years) incorporated into UO_2, to generate a localized α-field. The objective of the experiments were to mimic the radiation environment that would be experienced at the surface of aged spent nuclear fuel (SNF) during long-term geologic disposal under anoxic conditions.

Wittman et al. [2] predicted that in the presence of a pure α-radiation field and under H_2 conditions, the concentration of the radiolytic oxidant H_2O_2 would be suppressed or even eliminated. In a UO_2 corrosion experiment this would be exhibited through a lowering of the measured UO_2 corrosion potential compared to identical conditions in the absence of dissolved H_2. We found that the predictions of Wittman and co-workers were supported and that the corrosion potential of the ^{233}U-doped UO_2 in solution decreased in the presence of H_2 gas and increased in the absence of H_2, when under anoxic conditions. The PAMEC experiments indicate that H_2O_2 was eliminated in a solution sparged with H_2 while exposed to an α-radiation field. The corrosion potential of the α-doped $^{233}U(10\%)$- $^{238}UO_2$ in a solution sparged with Ar/H_2 matched the corrosion potential of $^{238}UO_2$ in solution sparged with air. This clearly demonstrated that the H_2O_2 had been eliminated and that the only oxidant present was O_2 in this system, which is in complete agreement with the modeling results of Wittman et al.

These results point to the need to improve the Fuel Matrix Degradation (FMD) Process Model training data set that is being used in the FMD surrogate model which is being developed for the repository program. The incorporation of realistic radiation chemistry will improve the scientific basis for the FMD Model.

Summary

The release of >95% of radionuclides from spent nuclear fuel (SNF) will be controlled by the dissolution rate of the uranium oxide (UO_2) fuel matrix. Under anoxic conditions the aqueous solubility of UO_2 would be exceedingly low; however, the self-generated radiolytic field will induce oxidizing conditions at the SNF-water interface that could result in corrosion. Repository designs, however, include a large amount of iron that are anticipated to corrode anoxically, resulting in the production of hydrogen (H_2) gas [3]. The Mixed Matrix Dissolution Model describes the interaction of these processes that would result in the significant reduction of SNF corrosion/dissolution rates [4].

A MATLAB™ version of Mixed Matrix Dissolution Model was developed by Jerden et al. [5] at Argonne National Laboratory, but this did not include all radiation chemistry processes, and therefore was unable to predict any direct interactions of the radiation field with H_2 and other components. New versions of the code are being developed by Mariner et al. [6] that will include these aspects of the radiation chemistry; however, even the current FMD model, excluding detailed radiation chemistry, is so complex that it has become computationally expensive to execute, given the large number of individual waste packages that need to be modeled in the repository. FMD surrogate models are being developed by Mariner et al. [6] from FMD process model training data to provide accurate matrix degradation rates in a repository simulation for each individual breached waste package in its own evolving environment at each time step. This machine learning approach is computationally more efficient than directly using the FMD chemical dissolution model. Hence, we can incorporate additional chemistry into the process model for developing training data and need not be concerned with the computational efficiency. For instance, fuel chemistry could be included in a new FMD process model, as well as improved radiation chemistry inputs. In the long run this approach would provide improved FMD surrogate models based on more accurate training data.

Wittman et al. [2] predicted that with a pure α-field, and in the presence of dissolved H_2, the radiolytic oxidant H_2O_2, would be almost eliminated, irrespective if UO_2 or any other material was present. The current FMD model relies entirely on the catalytic effect of Noble Metal Particles (NMP), whereas, many experiments have demonstrated that H_2 in solution would catalyze the decomposition of radiolytically generated H_2O_2 [7-10]. These effects are not included in the current FMD process model yet do play a significant role eliminating fuel oxidants.

Can experiments with SNF allow us to validate the FMD model? The SNF that is available for testing today contains ^{137}Cs and ^{90}Sr and generates a large β/γ-radiation field. These radioisotopes and resultant radiation field will be gone in ~300 years but are impossible to remove during any SNF test. What is their impact, and will these effects impede our ability to validate the FMD model? And how can we mitigate these effects and design experiments that can help to validate the FMD Model?

The solution is to construct experiments with materials that mimic the characteristics of aged SNF. In this report, we describe the production and testing of a micro-particle electrode consisting of a ^{233}U-doped UO_2 powder mixture. The radioisotope, ^{233}U, ($t_{1/2}$ = 160,000 yrs), is a high specific activity material that generates a strong α-field but a limited the β/γ-field owing to the high surface area to volume (SA/V) ratio of the powdered electrode of the PAMEC cell. The objective was to test the influence of α-irradiation with and without the presence of H_2 gas on UO_2 corrosion.

The microfluidic, 'particle-attached microfluidic electrochemical cell' device, or PAMEC, uses microgram quantities of uranium dioxide (UO_2) and allows us to observe electrochemical changes and measure properties [1]. The PAMEC device reduces the need for running experiments in a shielded facility. This novel design offers a platform to investigate SNF under aqueous environments and in the presence of gases, such as H_2, providing quantitative data on the corrosion processes and rates.

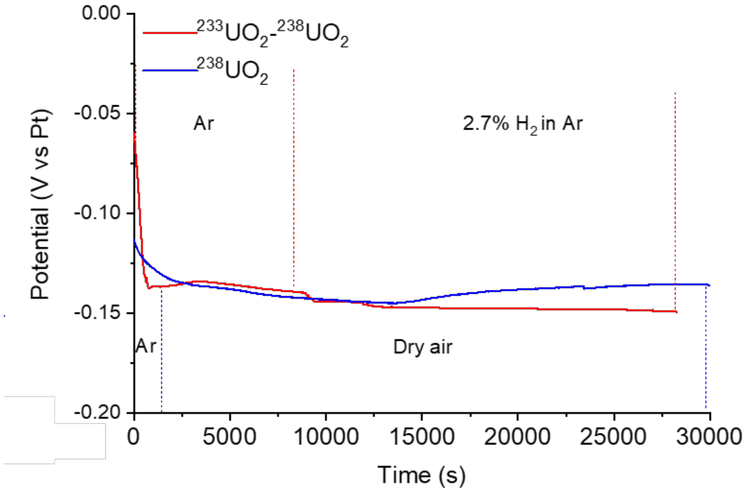

Wittman and co-workers have shown that the mere presence of an α-radiation field combined with dissolved H_2, can result in the destruction of H_2O_2 [2]. The experiments reported here support this prediction by Wittman et al. The corrosion of ^{233}U-doped UO_2 was lower in the presence of Ar/H_2 gas and matched that of $^{238}UO_2$ in a solution sparged with air (see Figure above), up until the inflection point, around 13000 s, when the $^{238}UO_2$-Working Electrode (WE) became passivated. This demonstrated that under an α-radiation field, and in the presence of dissolved H_2, the only oxidant remaining in the system is O_2. Again, this confirms the radiolysis modeling of Wittman et al. It is important to note that none

of these radiolytic effects are currently included in the FMD process model. Inclusion of the full radiolysis chemistry builds both accuracy and provides significant advantages for Performance Assessment (PA) calculations.

This report fulfills the *Inventory Waste Form Characteristics and Performance* Level 3 Milestone, *Report on Electrochemical Cells for SNF Model Validation*, M3SF-22PN010309051.

Acknowledgments

This work was supported by the U.S. Department of Energy Office (DOE) of Nuclear Energy, through the Office of Spent Fuel and Waste Science and Technology Research and Development Campaign (DOE NE-81) within the Office of Spent Fuel and Waste Disposition.

The authors thank Dr. Wes Lawrence and Ms. Wendy Erikson, Pacific Northwest National Laboratory (PNNL), for providing programmatic support and oversight. This document greatly improved by Cary Counts (PNNL Editor) and Dr. Susan E. Asmussen.

In addition, the authors thank Dr. Carlos Jove-Colon from Sandia National Laboratory for discussions. We thank Dr. Prasad Nair (DOE NE-81) for his continued interest in this research during the past year. Work was conducted at the PNNL Radiochemical Microscopy Q-suite. PNNL is operated by Battelle under contract DE-AC05-76RL01830.

Acronyms and Abbreviations

α	alpha
β/γ	beta/gamma
CE	Counter Electrode
CV	Cyclic Voltammetry
DI	Deionized water
DOE	U.S. Department of Energy
DOE-NE	DOE Office of Nuclear Energy
EBS	Engineered Barrier System
E-cell	Electrochemical cell
E_{corr}	Electrochemical Corrosion Potential
FMD	Fuel Matrix Dissolution Model
FY	fiscal year
KIT	Karlsruhe Institute of Technology
N/A	not applicable
NMP	Noble Metal Particles
OCP	Open Circuit Potential
PA	performance assessment
PAMEC	Particle-attached microfluidic electrochemical cell
PDMS	Polydimethylsiloxane
PVDF	Polyvinylidene fluoride
PNNL	Pacific Northwest National Laboratory
RE	Reference Electrode
ROI	Region of Interest
SA/V	Surface area to volume ratio
SALVI	System for Analysis at the Liquid Vacuum Interface
SE	Secondary Electron Imaging
SEM	Scanning Electron Microscopy
SFWST	Spent Fuel and Waste Disposition
SNF	Spent Nuclear Fuel
WE	Working Electrode
XPS	X-ray Photoelectron Spectroscopy

Units

eV	electron Volts
keV	kilo electron volts

mM	millimolar
µm	micrometers
s	seconds
wt %	weight percent
V	volts

Contents

Figures

Tables

1.0 Introduction

This report represents completion of the milestone deliverable M3SF-22PN010309051 "*Report on Electrochemical Cells for SNF Model Validation*." The report provides an update on the status of fiscal year (FY) 2022 activities for the work package SF-22PN01030905 for the DOE-NE Spent Fuel Waste Form Science and Technology (SFWST) Program.

1.1 Project Scope

During geologic disposal, the release of most radionuclides from spent nuclear fuel (SNF) will be controlled by the dissolution rate of the uranium oxide (UO_2) fuel matrix. A typical SNF under geologic disposal conditions, will emit 1000 alpha (α) -particles/mm^2/s. According to Pastina and LaVerne [11], each α-particle in water generates 5×10^4 molecules of the oxidant H_2O_2. Sufficient oxidants will be created during geologic disposal to completely oxidize the SNF. However, under the anoxic corrosion of iron (Fe), hydrogen (H_2) is produced that could impact this potential process [3]. The Fuel Matrix Dissolution (FMD) model developed by Jerden et al.[5] at Argonne National Laboratory assumes that the principal method of H_2 interaction with the oxidation of U^{4+} to U^{6+} will be through a catalytic process with Noble Metal Particles (NMP) embedded in the SNF (see Figure 1.1). The FMD model does not consider any aspects of radiation chemistry and therefore does not predict any direct interaction of the radiation field and H_2, or other species in solution. NMPs are believed to be ubiquitous in SNF UO_2 matrix and contain micrometer and nanometer particles, consisting only of Mo, Tc, Ru, Rh, and Pd. This catalytic process is the basis of the FMD model that may be used in any repository Performance Assessment (PA) calculations [5].

New versions of the FMD model are being developed by Mariner et al. [6] that will include these aspects of the radiation chemistry; however, the current model is sufficiently complex that has become computationally expensive to execute, given the large number of individual waste packages that need to be modeled in the underground repository.

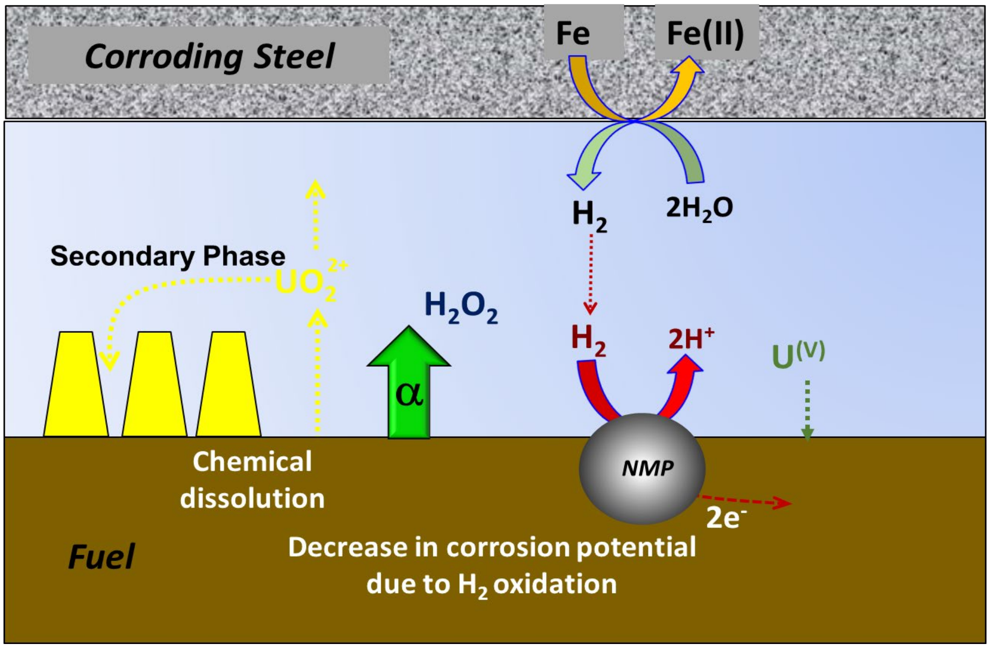

Figure 1.1 Schematic of processes in FMD Model. Radiolytic production of hydrogen peroxide (H_2O_2) leads to potential oxidation of SNF; however, H_2 gas from corroding Fe, interacts with Noble Metal Particles (NMP) on the fuel surface, resulting hexavalent uranium (U(VI)) reduction.

1.2 Improving the FMD Process Model

Mariner and co-workers are developing an interesting FMD surrogate modeling that could utilize FMD process model training data [6]. The computer simulation of the SNF dissolution process, (i.e., the FMD model) is designed to predict the repository physical behavior by solving a series of physical and chemical processes with mathematical equations. Currently, with the FMD process model, there are seven inputs parameters: temperature, burnup, time out of reactor[1], and the concentrations of CO_2^{3-}, O_2, Fe^{2+}, and H_2. We suggest that these inputs are deficient. For instance, O_2 is generated during radiolysis [12], but not included specifically in the current FMD model. There is also a strong indication that fuel composition will impact long-term behavior and that inclusion of such a term would benefit PA [13]. The composition of NMP is variable [14-16] and, it is unknown if all NMPs act in the same manner. However, the ability to include additional processes to date has been extremely limited owing to the computational requirements for the FMD process model. A machine learning approach to the model development will require:

---

[1] Both burn-up dependence and time out of reactor are used to calculate the dose at the surface. It is likely that ‘time out of the reactor’ in the case of geologic disposal would essentially be a constant.

- **sensitivity analysis**, to explore the changes in the degradation rate when the temperature, Fe^{2+}, etc., are varied.
- **optimizations**, to find perhaps the set of parameters that would result in the lowest or average degradation rate.
- **uncertainty quantification**, to calculate the probability of exceeding dose limits when specific parameters are uncertain (e.g., H_2 concentration).

In each case, this would require many simulations to be run. This factor has limited our ability to improve the FMD process model and its efficient implementation into PA. In surrogate modeling, a *statistical* (or *surrogate) model* is constructed to closely approximate the simulation, in this case the FMD output (see Figure 1.2).

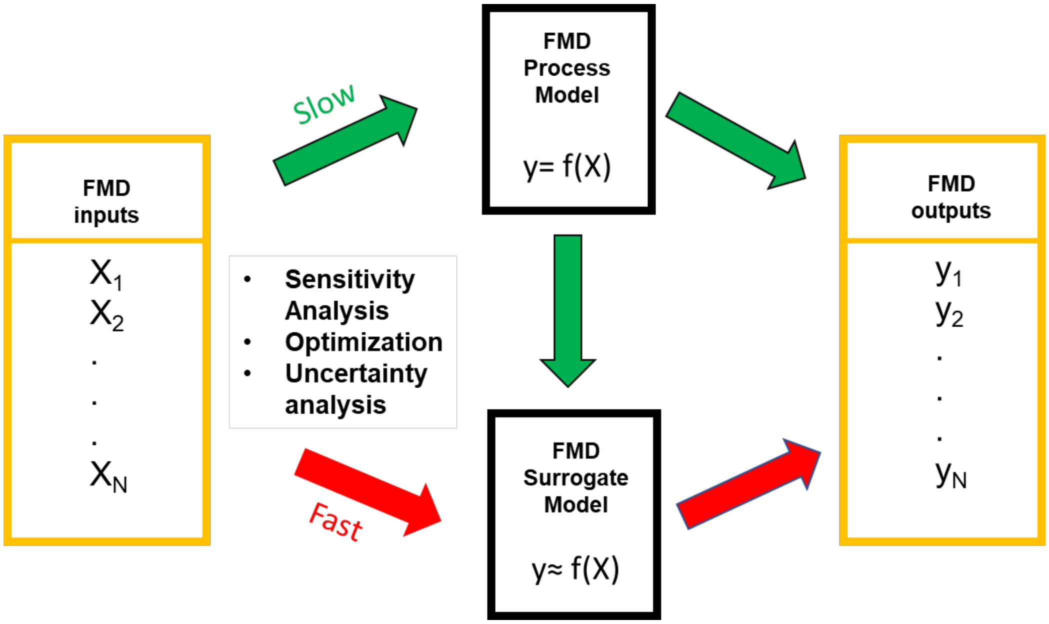

Figure 1.2 New approach to modeling SNF degradation rates provides the opportunity to improve the current physical and chemical inputs to the process model

The surrogate FMD model is trained using a data-driven approach where the training data is obtained via probing the simulation outputs at specific conditions within the parameter space (i.e, temperature, Fe^{2+}, etc.). At each of these locations in parameter space, a full simulation needs to be conducted to calculate the corresponding simulation output.

With this approach, degradation rates in a repository simulation for individual breached waste package, can be obtained efficiently. If the current FMD process model is improved by including more accurate radiation chemistry and chemical enhanced burn-up dependence, significant improvements to the overall model can be made. This is all made possible by the surrogate model approach.

1.3 Radiolysis Effects

An essential component in testing of nuclear materials is the radiation field. Many experiments do not include this vital characteristic and when this is included, it does not consider the influence of radiation quality (i.e., the presence of massive beta/gamma (β/γ)-fields in SNF) that will lead to erroneous results.

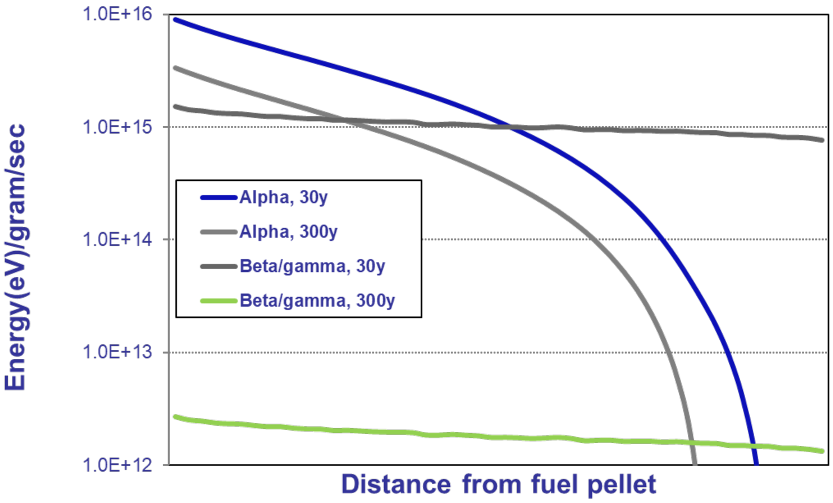

Figure 1.3 Effect of SNF age on radiation quality at the SNF surface (taken from [12], Figure 1.1)

Relatively fresh SNF has a different radiation quality and dose profile compared to aged SNF (see Figure 1.3). The α-dose impacts the near-field and modeling by Wittman and co-workers has demonstrated how this field will change in the presence of H_2 and other species. The large far-field β/γ-dose arising from fresh SNF will change the distribution of radiolytic species and may impact corrosion behavior.

Modeling by Wittman, Buck et al. [2, 17] has shown that during α-radiolysis, the partial pressure of H_2 in water results in suppression of H_2O_2 production (see Figure 1.4). This process was unique to α-radiation and is absent in a β/γ-field which yields additional radicals that destroy the agents that would otherwise react with H_2O_2 [18]:

$$H_2O_2 + e_{aq}^- \rightarrow OH- + \bullet OH \quad (1.1)$$

$$H_2O_2 + \bullet H \rightarrow H_2O + \bullet OH \quad (1.2)$$

$$H_2O_2 + \bullet OH \rightarrow H_2O + \bullet HO_2 \quad (1.3)$$

$$H_2O_2 + \bullet HO_2 \rightarrow H_2O + O_2 + \bullet OH \quad (1.4)$$

As the radical concentration increases, destruction of H_2O_2 increases, whereas, under a pure α-field, these radicals will be present in lower concentrations. When H_2 is introduced, through the anoxic corrosion of iron, the H_2 converts the •OH radical to the •H radical and accelerates H_2O_2 destruction through a chain reaction (reaction 1.5).

$$\bullet OH + H_2 \rightarrow \bullet H + H_2O \quad (1.5)$$

In other words, whereas the short-lived β/γ field will not yield significant H_2O_2, the long-lived α-field will, unless some external agent is introduced (e.g., H_2). O_2 can compete for •H radicals and disable H_2O_2 destruction (see Figure 1.4) [2, 17]. One question is whether O_2 that will be formed during these reactions (i.e., reaction 1.4) lead to UO_2 oxidation under these conditions?

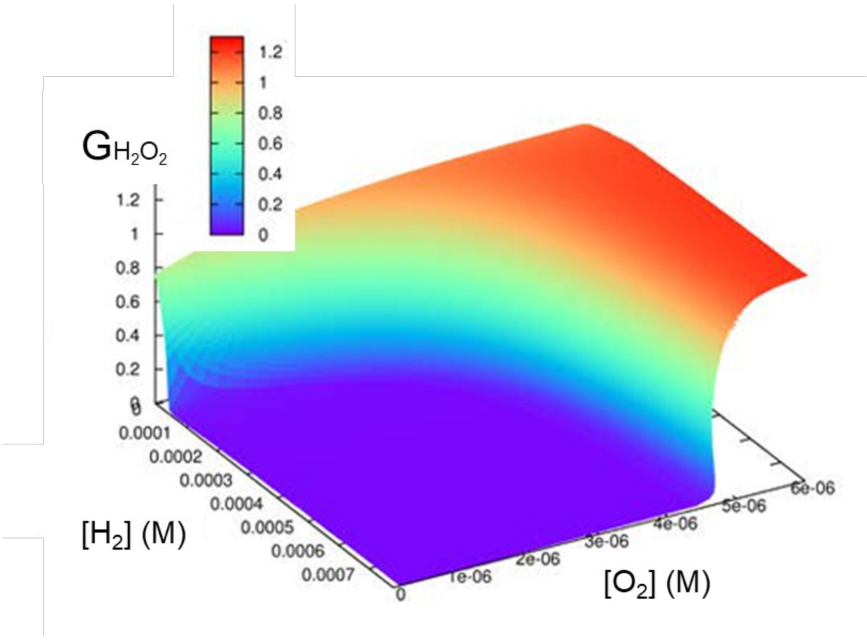

Figure 1.4 Dependence of $G_{H_2O_2}$ on $[O_2]$ and $[H_2]$ (adapted from [19]). By adopting FMD surrogate models, it will be possible to include these more complex aspects of radiation chemistry into the final degradation rate models.

Carbol et al. [9] and Ollila et al.[10] first used ^{233}U-doped UO_2 to study possible effects of α-radiolysis on the dissolution rate of UO_2. Tests conducted by Ollila et al. [10] used different

Surface Area-to-Volume (SA/V) ratios and at the lower SA/V (5 m^{-1}), no α-radiolysis was observed, whereas at high *SA*/*V* (15 m^{-1}) the dissolution rate was higher for the 10% ^{233}U-doped UO_2, suggesting the effect of α-radiolysis. Note to put these SA/V ratios into perspective: borosilicate waste glass dissolution tests can range from 340 m^{-1} on the low end for bulk samples, to 20,000 m^{-1} for powdered samples [20]. Ollila and co-workers suggested that a surface-catalyzed process was occurring in the H_2–UO_2–H_2O system, where H_2 was able to reduce oxidants originating from α-radiolysis.

Other species may be present in the repository environment that might need to be considered. In previous modeling studies, we also showed how halides impact this process and lead to increased H_2O_2 production [21]. The FEBEX study measured the gases produced in an anoxic disposal environment. Within 2 years, the O_2 disappeared but CO, CO_2, and CH_4 increased. Interestingly, N_2 remained high (~80%). Both N_2 and carbon-containing gases will undergo radiolytic-induced processes. N_2 will form nitric acid (HNO_3), and CO_2 can lead to the formation of oxalate. The HNO_3 will dissolve in the water with near infinite solubility. With co-disposal of waste forms (SNF and borosilicate glass) and high radiation field, a decrease in pH could occur that would impact glass dissolution rates. Wronkiewicz et al. [22] conducted tests to show that radioactive glasses will generate HNO_3, and this did speed up dissolution.

1.4 Noble Metal Particles

NMP are compositionally variable depending on fuel burn-up and location and typically occur as nanometer or micrometer particles [14, 23]. The noble metals sintered in synthetic UO_2 may not replicate the morphology of the SNF-derived NMP nor their composition. As of this time, the role of SNF-derived NMP have not been explored.

1.5 Flow Experiments

SNF degradation testing activities are ranked Medium-High Priority for the Spent Fuel Waste Form Science and Technology (SFWST) program [24]. Experiments with SNF are being considered to validate the overall processes and to determine the conditions under which the combination of H_2 generation from iron corrosion, H_2O_2 production, and catalytic NMP, control dissolution. However, there is one significant issue with this approach. The fuel that we have available for testing contains ^{137}Cs and ^{90}Sr that generates a large β/γ-radiation field (see Figure 1.3). These radioisotopes and resultant radiation field will be gone in ~300 years but is impossible to remove during any SNF test.

Micro-devices have two main advantages with respect to testing highly radioactive materials. First, the specimens are so small that experiments can be conducted outside shielded facilities, vastly reducing costs and, second, the high surface area to volume ratio of the material and small dimensions of the cell, means that experiments can probe the α-radiation field effect without the complexity of the short-lived β/γ-field. Figure 1.5 schematically describes the PAMEC (Particle Attached Microfluidic Electrochemical Cell) testing setup. With this gas and liquid flow setup, we can change the type of gas that is going to purge the electrolyte and keep the concentration of dissolved gas relatively constant during the electrochemical measurement. This differs from the SALVI cell [25] used previously in that there is no ability to use an ion beam for analysis due to a thicker Si_3N_4 window. Models have predicted that corrosion of SNF should be low under de-aerated/H_2 disposal conditions and significant secondary U(VI) phases should not form that are observed under oxidizing environments [26, 27]. However, if radiolysis generates oxidants, alteration phases might still form [28, 29], as well as sparingly soluble species or phases accumulating at the surface [30]. We have concentrated on analytical tools that can probe even small changes in surface chemistry, such as, x-ray photoelectron spectroscopy (XPS), rather than more bulk methods.

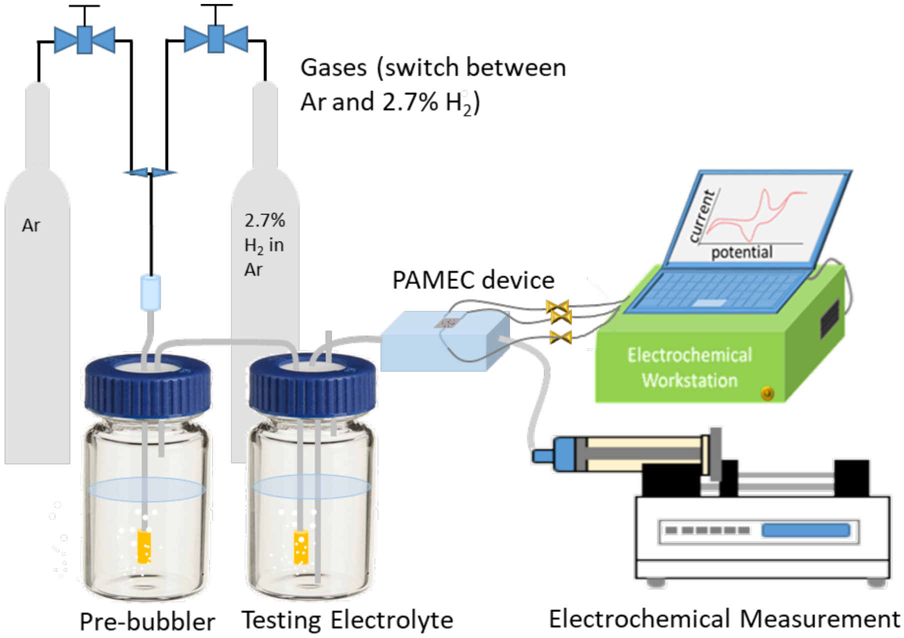

Figure 1.5 Schematic of gas and liquid flow setup for electrochemical measurement using PAMEC electrochemical cell

1.6 Impact to Future Modeling Efforts

The FMD Process Model requires further development to include aspects of radiation chemistry, the role of Fe(II), halides, etc., and the model lacks critical experimental data. Future endeavors need to address the role of NMP composition and morphology on H_2 suppression of SNF corrosion as well as the surface alteration that could impact the radiolytic field.

This report describes testing of the microfluidic devices with α-doped UO_2 in the presence of dissolved H_2 and under anoxic conditions, and fulfills the *Inventory Waste Form Characteristics and Performance* Level 3 Milestone, -*Report on Electrochemical Cells for SNF Model Validation*, M3SF-22PN010309051.

2.0 Development of Experimental Protocols

We are employing a new microfluidic electrochemical cell (PAMEC—Particle Attached Microfluidic Electrochemical Cell) to investigate UO_2 corrosion at the microscale. To demonstrate the power and flexibility of the PAMEC for measuring E_{CORR}, we performed initial experiments with two different working electrodes (WE) composed of Fe metal powder (Fe-WE) and hematite powder (Fe_2O_3-WE). The Fe_2O_3-WE was used to test the flow-thru PAMEC ultimately to be used with a $^{233\text{-}238}UO_2$-WE. We chose to work with Fe phases at this early stage because they are not radioactive and the redox couples are very well known.

2.1 Measurements with PAMEC E-Cell

Fe-WE (no flow): PAMEC devices were fabricated to measure the E_{CORR} of Fe. Fe-powder (Sigma-Aldrich, <10 µm powder) was mixed with polyvinylidene fluoride (PVDF)/carbon black and N-methyl-2-pyrrolidone to form the slurry. 1µL of this slurry was applied to make Fe-WE. The detailed fabrication procedure of using PVDF/CB to make the PAMEC device was described previously [1]. 0.1M $NaClO_4$ (pH=9.5) was purged with N_2 for 30 minutes before the corrosion potential measurement.

Figure 2.1 shows the influence of cathodic pretreatment (E_{PRE}) on the E_{CORR} of the working electrodes made of Fe powder. For the Fe-WE, without being cathodically pretreated, the values of E_{CORR} were higher than the ones of the Fe-WE cathodically cleaned for ten minutes. After applying negative potentials (E_{PRE} = −1.2 V or −1.5 V) on Fe-WE, the values of E_{CORR} (red and blue lines in Figure 2.1) were more negative than the untreated Fe-WE (black line in Figure 2.1). The E_{CORR} measured after pretreatment at -1.5V were significantly lower than the untreated one. The E_{CORR} measured after pretreatment at -1.2V was lower than the untreated WE before 350 seconds but increased with time approaching the value for the untreated Fe-WE. This demonstrated that the cathodic reduction preformed at Fe-WE was reversible. If given a longer measurement time, e.g., 500 minutes, the E_{CORR} of Fe-WE pretreated at -1.5V may have increased to reach the E_{CORR} of untreated one.

These experiments demonstrated the feasibility of using this new microfluidic electrochemical cell (PAMEC) in studying the corrosion potential of microgram quantities of material.

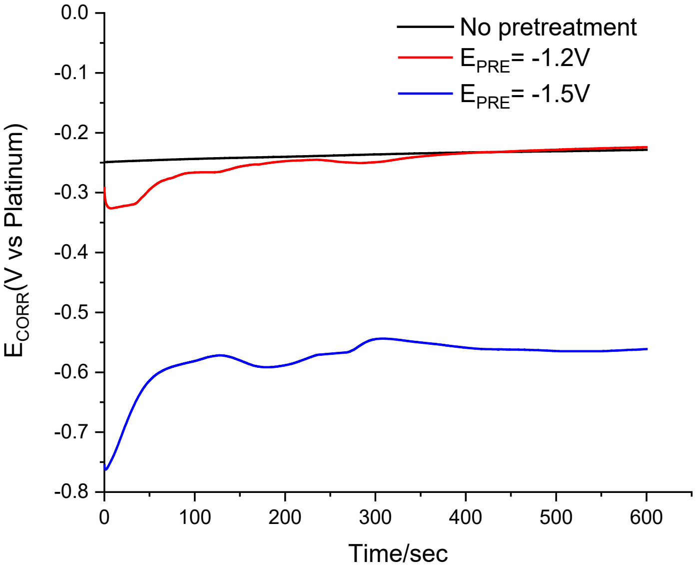

Figure 2.1 The corrosion potential of Fe WE in 0.1M $NaClO_4$ (pH=9.5). The electrode was cathodically pretreated (E_{PRE}) at -1.2V, -1.5V for 10 minutes, respectively, comparing to untreated one.

Fe_2O_3-WE (flow thru): Next, we developed a system that can flow gas-sparged solutions through the PAMEC and that included a radiation source (i.e., $^{233}UO_2$). The system was completed and set-up inside a radiation-contained environment (see Figure 2.2). The primary objective was to flow H_2 sparged solutions into the PAMEC cell containing the UO_2 electrode. The protective clean-box shown in Figure 2.2B enabled us to work with the ^{233}U source and included inlets for H_2 and discharge to a fumehood. The selected gas (e.g., inert gases (N2 or Ar), or H2 mixed with inert gas, (Figure 2.2A) is introduced to a glass bottle labelled as pre-bubbler to saturate the gas with testing solution vapors (Figure 2.2B). This helped reduce the loss of solution due to evaporation during the sparge process. The saturated gas then is introduced into the second glass bottle filled with testing electrolyte (e.g., 0.1M NaClO4, pH=9.5). After the oxygen is removed from the testing electrolyte and the electrolyte is saturated with the selected gas, the syringe pump (Figure 2.2C) withdraws the electrolyte from the testing electrolyte vial through the PAMEC device during the E_{corr} measurement (Figure 2.2D).

A notable modfication made in this system was the programmable syringe pump that we used to pull liquid through the system and keep the flow at a steady constant rate. This prevented the formation of bubbles in the microfluidic system. The programmable syringe pump was used to vary flow rates and maintain the system for >30 hours when measuring the corrosion potential.

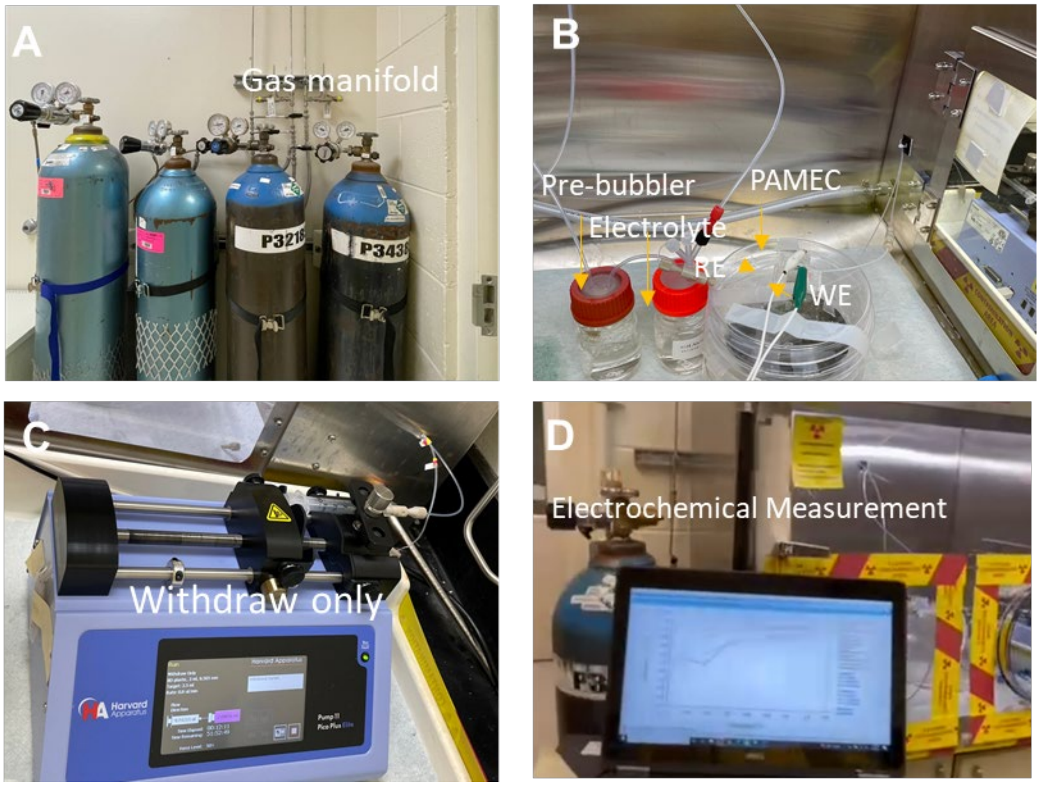

Figure 2.2 Photographs of (A) gas manifold, (B) gas introduction though Teflon tubing and liquid flow design for testing PAMEC containing UO_2 electrode, (C) syringe pump for controlling the flow rate, and (D) electrochemical measurement data acquisition.

To test the gas and flow system setup, we applied an Fe-WE using PAMEC to record the E_{corr}. In Figure 2.3, the output result was acquried from an Fe-attached WE in an electrolyte (0.1M $NaClO_4$ (pH=~8.0)) purged with H_2 when E_{corr} recording started. The plot displays E_{corr} vs Pt standard electrode. The E_{corr} decreased with time showing the effect of dissolved H_2 in the electrolyte. In region I, (0s -120s), the E_{corr} dropped due to the increase of anodic reaction at Fe-WE. In region II (120s-640s), the E_{corr} increased, possibly attributed to the passive oxide film formed on the Fe-WE electrode due to the dissolved O_2 in the freshly prepared $NaClO_4$. In region III (640s-2900s), the E_{corr} fluctuated but showed a decreasing trend due to the competing effects from dissolved O_2 and H_2. Finally, in region IV (2900s-6400s), the E_{corr} dropped significantly indicating the reducing effect resulting from increasing dissolved H_2/O_2 ratios as O_2 was progressively removed from the solution due to H_2 purging.

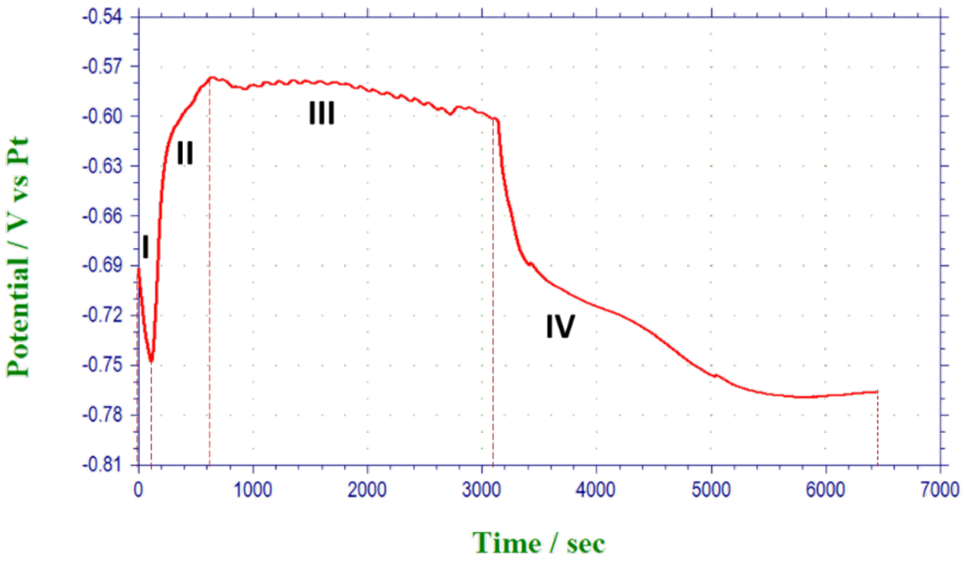

Figure 2.3 E_{corr} of Fe-WE in the electrolyte purged with H_2

In sum, the flow rate did not affect the cyclic voltammograms significantly and H_2 was successfully introduced into the PAMEC device without the formation of bubbles. Lastly, the corrosion potential (E_{corr}) responded robustly to dissolved O_2 and H_2 in the electrolyte.

2.2 Characterization Methods

XPS was performed on a Kratos AXIS Ultra DLD system using a monochromatic Al-K_{α} source (h*v*= 1486.7 eV) operating at an analysis chamber pressure of < 2 × 10-9 Torr. The intact PAMEC devices were transferred into an inert glove box attached to the fast entry port of the XPS instrument. The cells were disassembled under an Ar atmosphere (O_2 at <2 ppm) and mounted onto conductive copper tape for analysis.

In-situ electrochemical testing and imaging of the PAMEC cell was performed in the chamber of a FEI Quanta 250FEG Environmental SEM with electrical feed-throughs.

3.0 PAMEC Electrochemical Testing of Aqueous and Solid Uranium Species

In the previous funding-cycle we demonstrated that the PAMEC could reproduce the CV of $^{238}UO_2$ from bulk measurements. As discussed in section 2.0, this year, we expanded the capabilities of the PAMEC to handle 1.) flowing fluids sparged with different gases, and 2.) the highly radioactive isotope ^{233}U. The new set up was then tested with Fe- and Fe_2O_3-WEs with good success. In the following subsections we describe results for uranium using the new PAMEC capabilities.

3.1 CV Aqueous Uranium

To demonstrate the versatility of the PAMEC (i.e., can it provide accurate results for aqueous U as well as for solid forms), we tested a 0.31 mM $UO_2(NO_3)_2$ in 50 mM acetate buffer and 0.1 M KNO_3 (pH=3) using the PAMEC blank device (i.e., the WE) which was made of the PVDF/CB composite w/o UO_2) (Figure 3.1). Cyclic voltammetry (CV) was performed at 100 mV/s, which was the same as that reported in the literature. The potential was recorded from a Pt wire reference electrode (RE). Peled and co-workers [31] used an Ag/AgCl RE where we used a Pt RE. The difference between the Pt electrode from the PAMEC and Ag/AgCl electrode was measured by using the Pt wire electrode as the WE and Ag/AgCl electrode as the RE in 0.1 M KNO_3 and 50 mM acetate buffer (pH=3). A constant reading of ~0.48V was obtained for ~8000s (Figure 3.2).

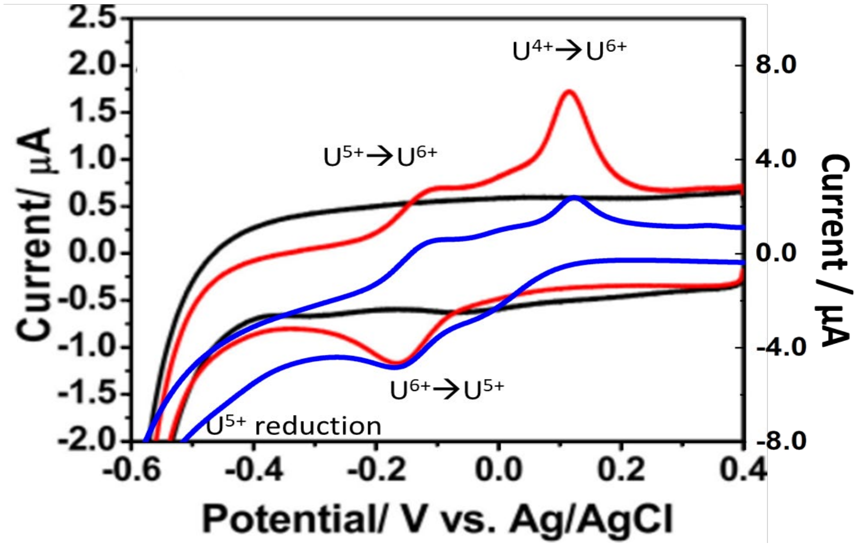

Figure 3.1 The cyclic voltammogram of 0.31mM UO_2^{2+} in 50 mM acetate buffer and 0.1 M KNO_3 (pH=3) (blue) recorded from PAMEC after potential shift correction, and cyclic voltammogram of the background (black) and 0.1 mM (red) of UO_2^{2+} in 50 mM acetate buffer and 0.1 M KNO_3 (pH 3) recorded with a gold macroelectrode from the reference*[31]*. All results were obtained at 100 mV/s scan rate. Left Y axis

corresponds to the results from the reference, and right Y axis corresponds to our result from PAMEC.

The potentials obtained from the PAMEC blank device (blue curve in Figure 3.1) were converted to the Ag/AgCl scale to facilitate comparison of electrochemical measurements. The experiments were conducted at 20 ± 1 ˚C. The oxidation and reduction of one electron transfer of UO_2^{2+} were seen and reported at E=-0.162 V and E=-0.119 V versus Ag/AgCl [31], which can be explained in Equation 3.1. We observed the same one-electron associated oxidation and reduction peaks at -0.114V and -0.173V, respectively, after potential shift correction (blue curve in Figure 3.1). The second reduction wave starting at ~ -0.30 vs Ag/AgCl was observed in our measurement, which can be attributed to the reduction of UO_2^{+} to the insoluble species UO_2 (Equation 3.2), although it is masked by the larger reduction wave of H_2O to H_2 (Equation 3.3). This observation was consistent with the literature as well. Further, the second oxidation peak occurred at E=0.121V vs Ag/AgCl (-0.115V in the literature), which is associated with the two-electron oxidation of UO_2 to soluble species UO_2^{2+} (Equation 3.4).

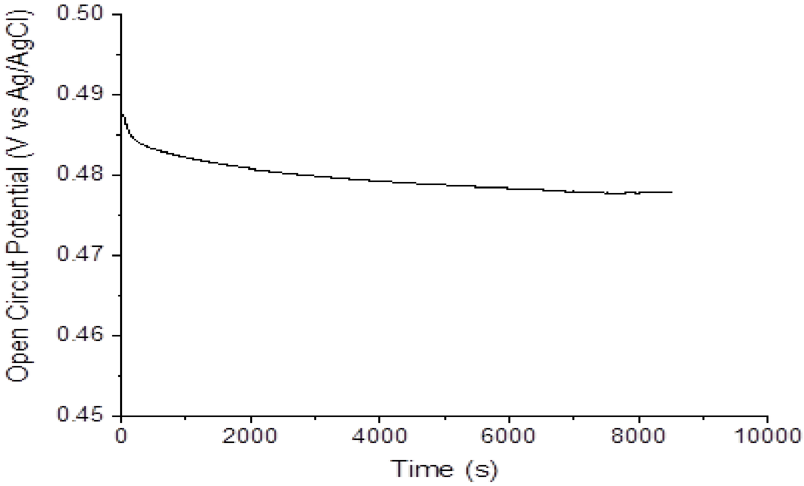

Figure 3.2 Measurement of potential difference between Pt electrode and Ag/AgCl reference electrode in 0.1 M KNO_3 in 50 mM acetate buffer (pH=3). A constant reading of about 0.48 V was obtained for ~8000s.

Overall, the redox of uranyl species were observed in the PAMEC and the results were in good agreement with the published data, although the peak current values were higher than the ones in the literature, because we tested higher concentration of uranyl nitrate (0.31 mM vs 0.1 mM). This further validates the performance of PAMEC microfluidic electrochemical cell in the application of studying radioactive samples, and its versatility in investigating both particle materials and soluble species in solution.

$$UO_2^{2+} + e^- \leftrightarrow UO_2^+ \tag{3.1}$$

$$UO_2^+ + e^- + 4H^+ \leftrightarrow U^{4+} + 2H_2O \tag{3.2}$$

$$2H_2O + 2e^- \rightarrow H_2 + 2OH^- \tag{3.3}$$

$$U^{4+} + 2H_2O \rightarrow UO_2^{2+} + 2e^- + 4H^+ \tag{3.4}$$

3.2 Fabrication of ^{233}U-doped ^{238}U Electrode PAMEC

We synthesized a ^{233}U-doped UO_2 material for the electrodes in the PAMEC device (see Figure 3.3). The uranium isotopic composition was quantified with gamma spectroscopy. $^{233}UO_2$ was present at ~7.9% in the $^{233}UO_2$ -$^{238}UO_2$ mixture (see Table 1 and Table 2).

CAUTION !
The ^{233}U isotope of uranium are radioactive and inherently pose a radiological hazard. Experiments with these elements should only be performed by trained staff in a facility equipped to safely handle radioisotopes.

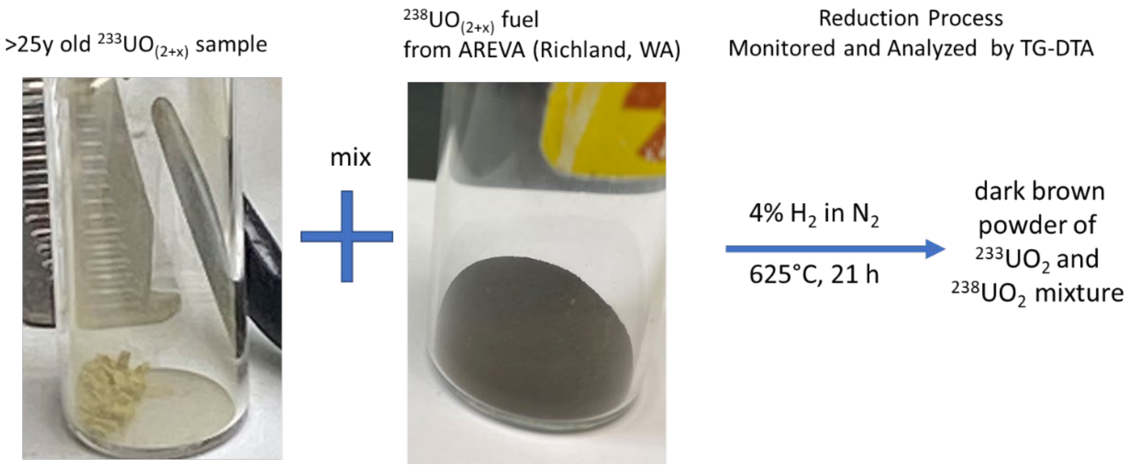

Figure 3.3 Photographs of the ^{233}U powder and the formation of the mixed oxide for the PAMEC cell

The formation of the activated powder required reduction in H_2 at high temperature. The thermogravimetric analysis (TGA) is shown in Figure 3.4. In total, 9.65% mass was lost during the reduction process. The time taken for the system to reduce was significantly longer than anticipated. This is an interesting observation that needs closer attention. One reason why a ^{233}U oxide might take longer to reduce than a less active form would be radiolysis. In a nutshell, this experimental procedure is mimicking many of the important aspects of the overall goals of the project. How much more difficult are oxidation/reduction processes in the presence of a radiation field and overpressure of H_2? Is there competition between radiolytic species being generated at the surface and H_2 diffusing from outside? It is interesting to speculate, whether NMP would have sped up this reduction process.

Table 1 Radiochemical results on the UO_2 powder containing ^{233}U

Element	**$t_{1/2}$ (a)**	**Bq/sample**	**+/-**
U233	1.59E+05	9.66E+05	6.90E+04
U235	7.04E+08	1.12E+01	2.67E+00
U238	4.47E+09	3.99E+02	6.24E+01

Table 2 Determination of ^{233}U content in oxide

Element	**Grams/sample**	**+/- %**	**UO2**	**Mass (g)**	**Mass %**
U233	2.71E-03	7%	$^{233}UO_2$	3.08E-03	7.9%
U235	1.39E-04	24%	$^{235}UO_2$	1.58E-04	0.4%
U238	3.14E-02	16%	$^{238}UO_2$	3.56E-02	91.7%
Total (g) of element U	3.43E-02		Total (g) of UO_2	3.89E-02	

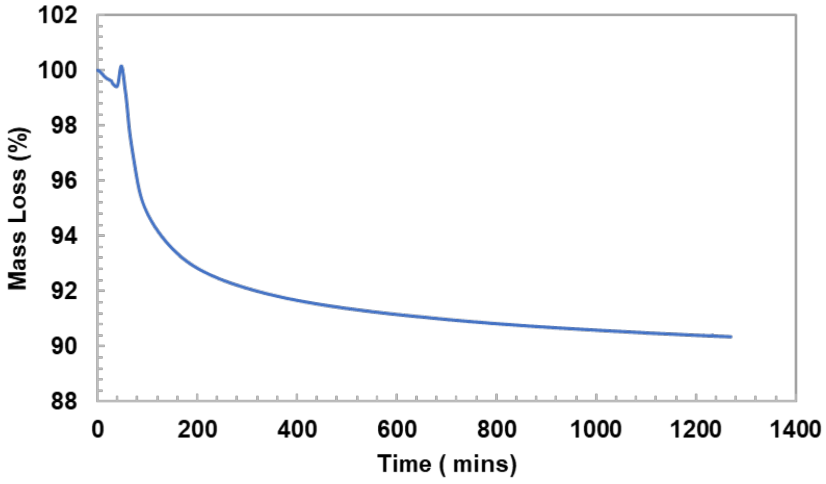

Figure 3.4 Mass loss with time for the formation of the UO_2 powder containing ^{233}U

Following the reduction, the $^{233}UO_2$ - $^{238}UO_2$ mixture had a mass of ~48.4mg which was sufficient for the planned experiments. The surface area of the UO_2 is critical for improving the performance of the device. We examine the $^{238}UO_2$ powder with SEM (see Figure 3.5). This data was collected under automated mode and the results used to determine the surface morphological characteristics of the particles (see Figure 3.6). Based on rough imaging, it was clear that there were large agglomerates, sometimes exceeding 20-30 µm, composed of much smaller particles. The particles were examined with an EDAX™ (EDAX Inc., Mahwah, NJ) automated particle analysis system on the SEM.

To avoid artifacts, all particles with aspect ratios over 7 were excluded. This was done to avoid instrument errors where particles are bisected during the image analysis or too many particles had been artificially made into one particle. Most of the particles were clearly round. This analysis was accomplished with python scripts and the data plotted with various python packages.

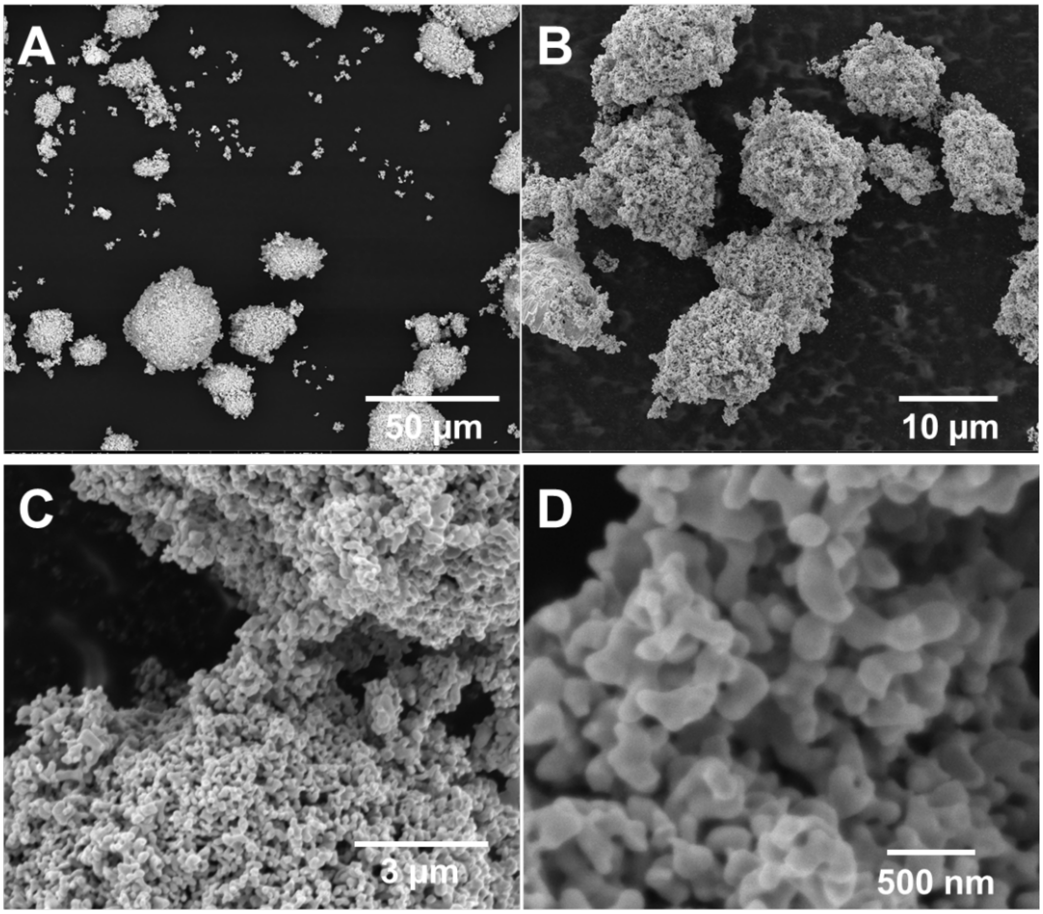

Figure 3.5 SEM images of the UO_2 powder (non-^{233}U containing)

Although the electrode in the PAMEC devices contains small particles, the SA/V of the UO_2 was moderate. The internal volume of the PAMEC was ~4.6 µL and the mass of UO_2 in the PAMEC device was ~7.0 µg. With an estimated average particle diameter of 2.0 µm this gives an estimated SA/V of ~460 /m.

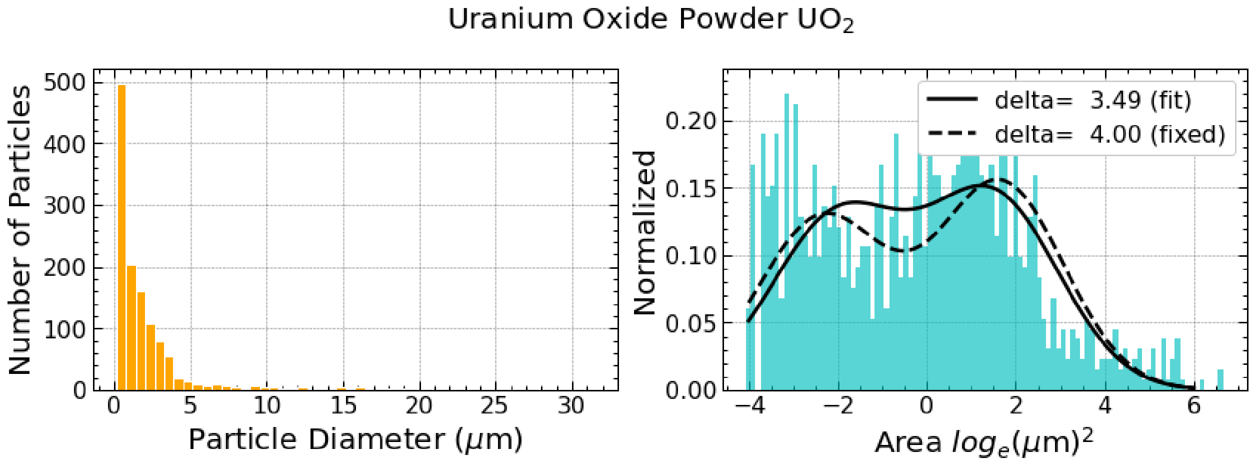

Figure 3.6 Particle analysis of UO_2 from SEM results showing a bimodal distribution of particles

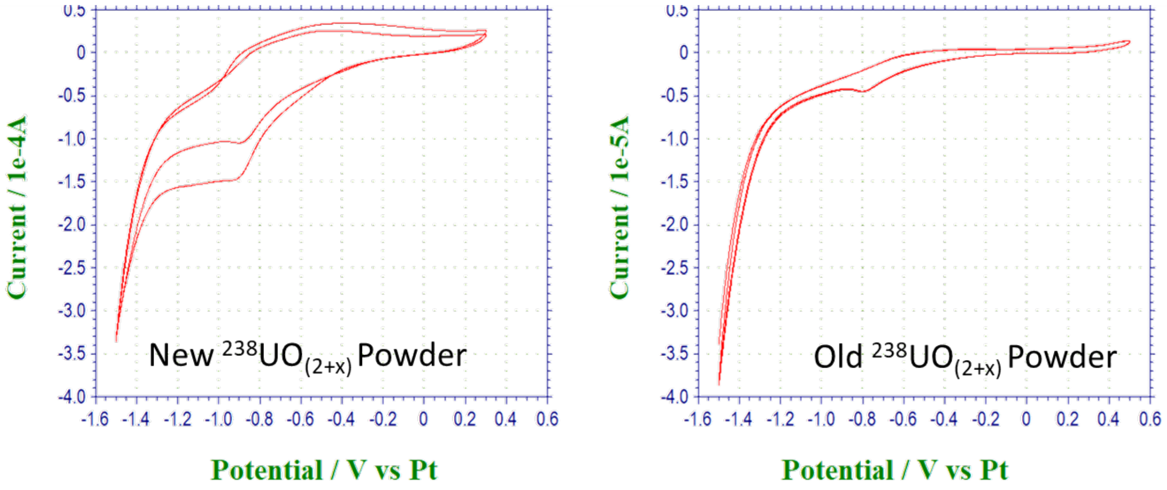

Figure 3.7 The electrochemical results from the newly prepared powder compared with earlier versions. Electrolyte: 0.1M $NaClO_4$ (pH=~9.5) and the scan rate was 100mV/s. By increasing the surface area of the particles, it was possible to observe the oxidation state changes conclusively.

Comparison of testing a PAMEC cell with a $^{238}UO_{(2+x)}$ -WE (prepared in the same way as the $^{233\text{-}238}UO_{2\text{-}x}$-WE) to results using our previous $^{238}UO_{2\text{-}x}$-WE (see Figure 3.7) indicates that the new higher surface area WE yielded an appreciably stronger response.

Figure 3.8 shows that the corrosion potential of two uranium oxide materials, an as-received material (UO_{2+x}) (blue curve) and a reduced material (UO_2) (red curve), that was reduced by a thermogravimetric experiment possess lower corrosion potentials than an oxidized material, as expected. However, demonstrating this process on a microfluidic cell is a significant advancement over bulk methods.

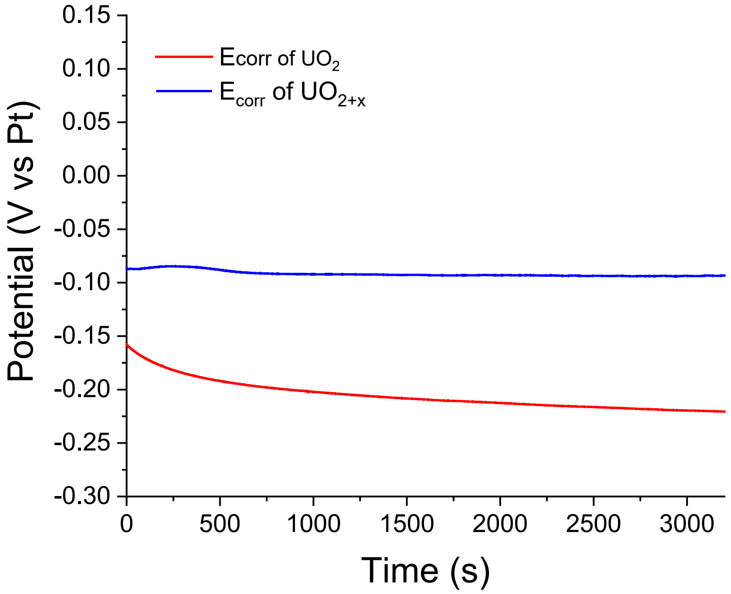

Figure 3.8 UO_2 electrode shows lower E_{corr} than UO_{2+x}, i.e., ~-0.22 V vs -0.09V vs Pt)

The electrolyte used in the experiment was 0.1M $NaClO_4$ (pH=9.5) and no pretreatment was performed on the UO_2 electrode, (e.g., cathodic cleaning or anodic corrosion). The UO_2 electrode exhibited a lower corrosion potential (E_{corr}) than oxidized form (UO_{2+x}), i.e., ~-0.22 V vs -0.09V vs Pt.

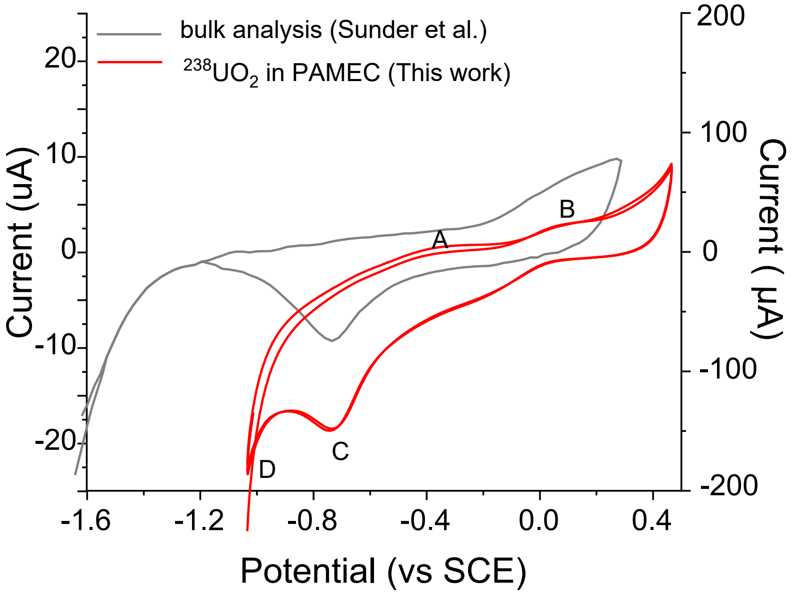

Figure 3.9 Cyclic voltammograms comparison at 20 mV s^{-1} scan rate, with left Y-axis corresponding to our result using PAMEC microelectrode of $^{238}UO_2$ (red line), and with the right Y-axis corresponding to the bulk analysis result reported by Sunder et al. (grey line), after potential shift correction from Pt reference electrode to SCE.

Figure 3.9 shows the cyclic voltammograms comparison between bulk analysis and microelectrode from PAMEC. The same testing solution (0.1M $NaClO_4$, pH=9.5, purged with inert gases before use) was applied. In region A (red curve), the anodic peaks are observed, which may have resulted from sub-monolayer oxidation of the surface. The main surface oxidation process can be seen in region B, prior to extensive oxidative dissolution at E>0.3 V vs. SCE. Region B corresponds to the oxidation of the UO_2 surface to approximately $UO_{2.33}$. Process C results from the reduction of the $UO_{2.33}$ layer back to UO_2 or UO_{2+x}. Region D results from the reduction of water (with H_2 evolution) [32]. Because the RE used in PAMEC is platinum, the cyclic voltammograms obtained from PAMEC were converted to the potential vs SCE.

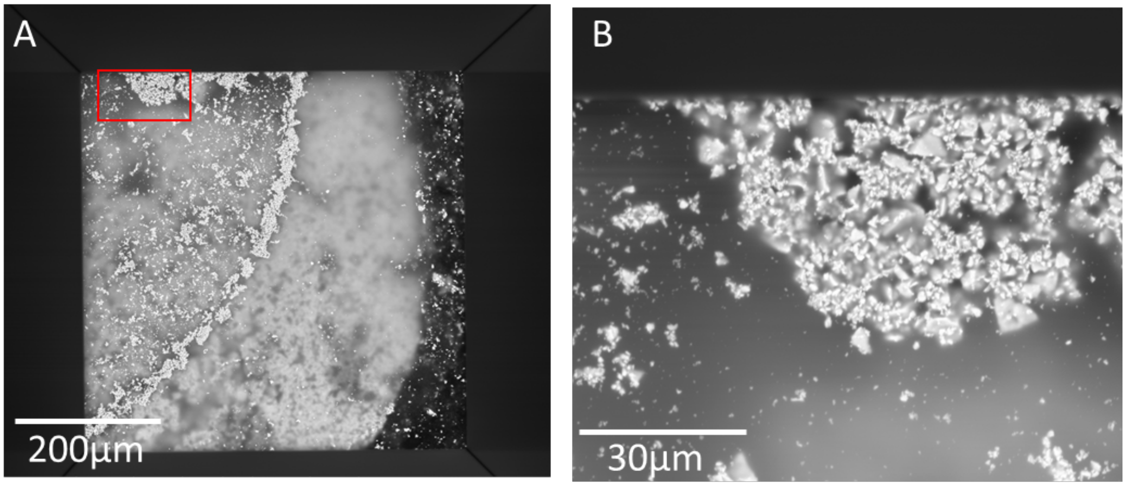

Figure 3.10 in situ SEM imaging of $^{238}UO_2$ electrode attached under the PAMEC detection Si_3N_4 window membrane (A), and (B) the higher resolution imaging at the UO_2 particles in the red box area highlighted in (A).

Figure 3.10 demonstrates another unique feature of PAMEC, in situ SEM imaging, enabled by its 50 nm thick Si_3N_4 detection window. PAMEC is a vacuum-compatible device that allows the direct imaging on the WE, UO_2 in this case, using a high-resolution imaging technique, SEM. This feature enables real-time observation of microstructural changes during the corrosion process of UO_2 when it is in contact with liquid. This advantage can also facilitate other analytical techniques for real-time investigation, such as the chemical state evolution during the corrosion process using X-ray absorption spectroscopy (XAS).

3.3 Effect of H_2, in Ar or N_2, with an α-Radiation Field under flow conditions

A 0.1M $NaClO_4$, solution at pH=9.53 sparged with N_2 or 4% H_2/N_2, was flowed through the PAMEC at 0.8 µL/min. The difference in E_{corr} between the ^{233}U-doped UO_2 and $^{238}UO_2$ electrodes is shown in Figure 3.11, one can see the effect on E_{corr} with use of the ^{233}U electrode versus a ^{238}U electrode. Under N_2, the steady state E_{corr} for ^{233}U-doped UO_2 was higher than E_{corr} for $^{238}UO_2$ (region I vs region i), which is likely attributed to the oxidants produced by ^{233}U α-radiation, e.g., H_2O_2. Switching to H_2 sparging decreased the E_{corr} of ^{233}U-doped UO_2 (region II) after a lag.

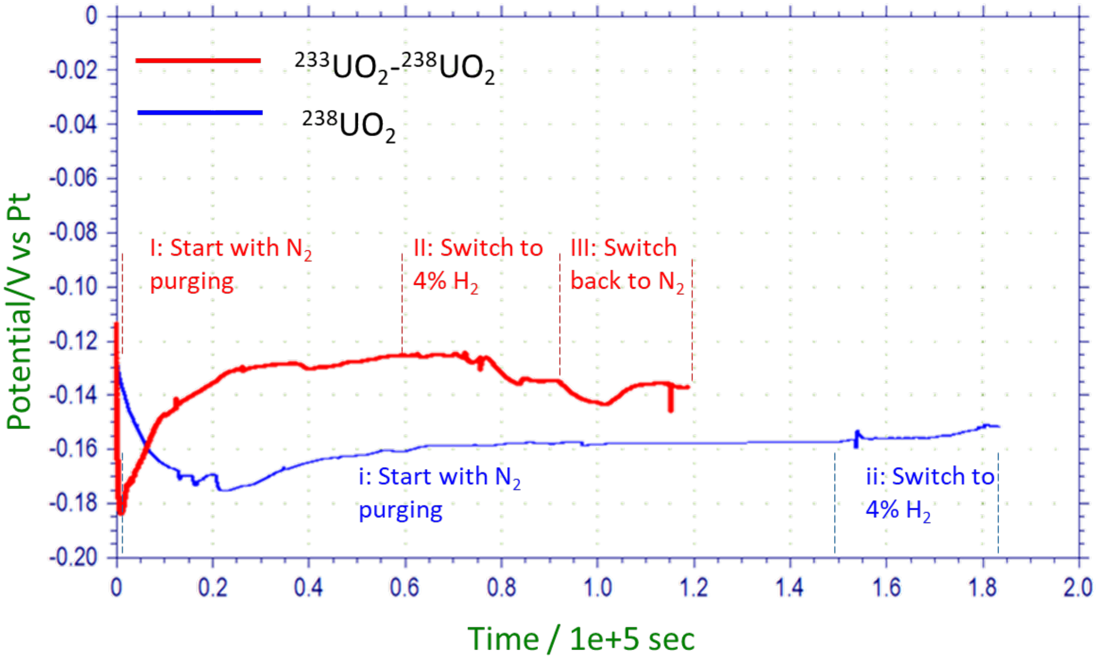

Figure 3.11 E_{corr} comparison between $^{233}UO_2$-$^{238}UO_2$ (red curve) and $^{238}UO_2$ (blue curve) electrodes shows different responses to dissolved H_2 in solution.

The E_{corr} did not immediately reflect the change of the gases. This delay likely reflects the finite time it takes the solution to reach the PAMEC reservoir from the gas-purged electrolyte bottle. The increase of E_{corr} after switching back to N_2 (region III) confirmed the effect of dissolved H_2 on H_2O_2 production (the major oxidant) in the α-irradiated UO_2 electrode (^{233}U-doped UO_2). In contrast, there was no significant difference in the steady state of ^{238}U UO_2- E_{corr} measured in the N_2 (region i) or H_2 purged electrolyte (region ii).

The final pH decreased to 9.01 which may be due to the formation of HNO_3 from radiolysis of dissolved N_2. Consequently, we re-ran experiments with Ar and 2.7% Ar/H_2.

To resolve some of the potential issues with N2 gas in a radiation field, experiments were run using Ar/H_2 with the α-doped ^{233}U-UO_2 and with sparged air with the non-doped $^{238}UO_2$ electrodes. The E_{corr} was measured for ^{233}U-doped UO_2 (Figure 3.12A) electrode and $^{238}UO_2$ electrode (Figure 3.12B) separately, recording the evolving surface potential of the UO_2 electrode in the gas-purged electrode as a function of time. In both measurements, the electrolyte (0.1M $NaClO_4$, pH=9.5) was purged with Ar for 30 minutes prior to the E_{corr} measurement. Figure 3.12A depicts the E_{corr} of ^{233}U-doped UO_2 in the electrolyte that was purged with Ar for ~2.5 hrs. and then switched to 2.7% H_2 for 5 hrs. The E_{corr} of ^{233}U-doped UO_2 decreased at very beginning from -0.06 V to -0.14 V vs Pt reference electrode, which is likely attributed to the increase in the anodic reaction of UO_2

due to the remaining oxygen on the electrode surface. The E_{corr} of ^{233}U-doped UO_2 reached steady state at ~9000s (2.5 hrs) and then it decreased after Ar/2.7%H_2 was introduced into the electrolyte.

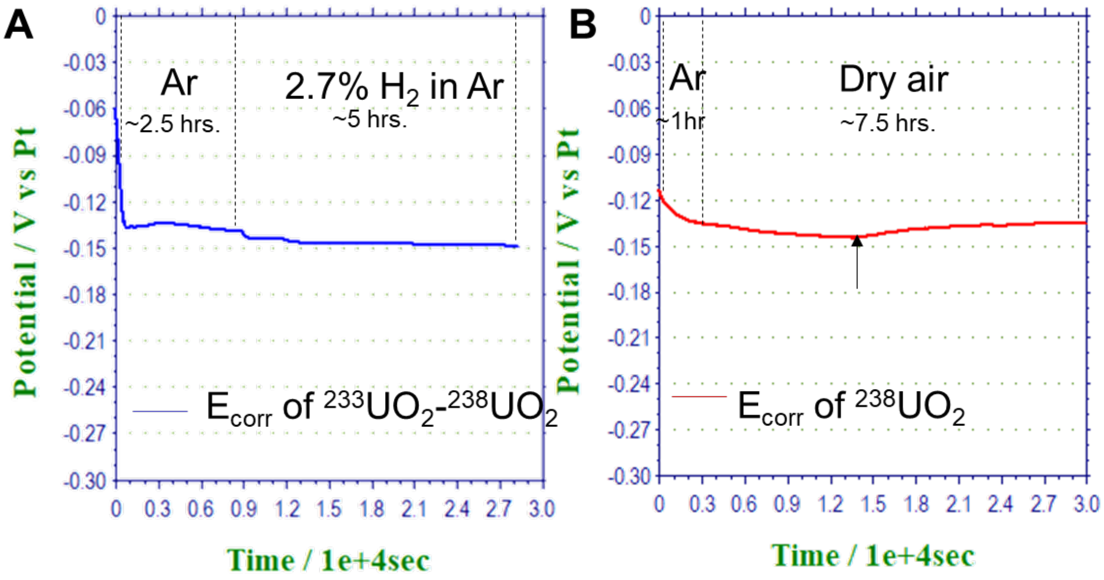

Figure 3.12 E_{corr} of (A) $^{233}UO_2$-$^{238}UO_2$ electrode and (B) $^{238}UO_2$ electrode exposed in the electrolyte purged with different gases.

The E_{corr} was steady after 5 hrs of H_2 purge and reached at ~-0.15V vs Pt, demonstrating the reducing effect of dissolved H_2 on the α-irradiated UO_2 surface. In comparison, the E_{corr} of $^{238}UO_2$ (Figure 3.12B) decreased at the beginning (-0.12 V to -0.13 V vs Pt) due to the increase of anodic reaction even with the continuous Ar purging until ~1 hr. Then the electrolyte was purged with dry air for ~7.5 hrs. The E_{corr} kept decreasing under this condition until reaching -0.14 V vs Pt, as marked by the back arrow. This may be explained by the anodic reaction of UO_2 due to the introduce of O_2-containing air sparging. However, with the passive oxide film accumulated on the electrode over time, it led to the decrease in the anodic reaction. It is manifested by the increase of Ecorr from ~13,000 s to the end of the E_{corr} measurement.

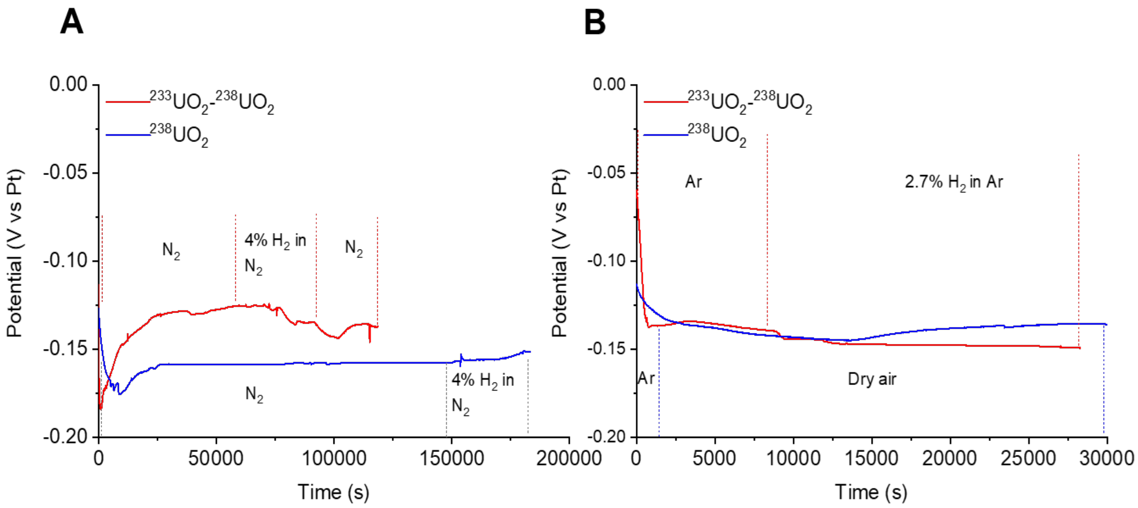

Figure 3.13 Comparison of E_{corr} in different conditions demonstrating the impact of the α-radiation field and H_2 sparging. (A) The highest E_{corr} was observed with ^{233}U with N_2 gas sparging and the lowest with ^{238}U and N_2 or N_2/H_2 gas sparging. (B) In contrast, the Ecorr of ^{238}U in dry air matched the E_{corr} of ^{233}U with H_2 gas sparging, lying between the E_{corr} in (A) and indicating that O_2 is the remaining oxidant in the system.

In Figure 3.13, several E_{corr} curves have been overlaid to show the effects of the various conditions. The clear result from these experiments is that α-radiolytically generated H_2O_2 in solution is eliminated by dissolved H_2. This directly supports the modeling study of Wittman et al. that first proposed this effect to occur exclusively with α-radiation [2]. A notable result is that E_{corr}, and its rate of decrease, for ^{233}U-doped UO_2 in solutions sparged with H_2 matches the rate for $^{238}UO_2$ (non-doped) in air-sparged solutions up until the likely formation of a passivation layer on the $^{238}UO_2$-WE (marked by the inflection point around 13000 s in Figure 3.13B). This suggests that the only oxidant remaining in the system is O_2 which again agrees with the radiolysis model of Wittman and co-workers. None of these effects are currently included in the FMD process model as developed by Jerden et al.[5]. Consequently, the current FMD process model will lead to erroneous conclusions.

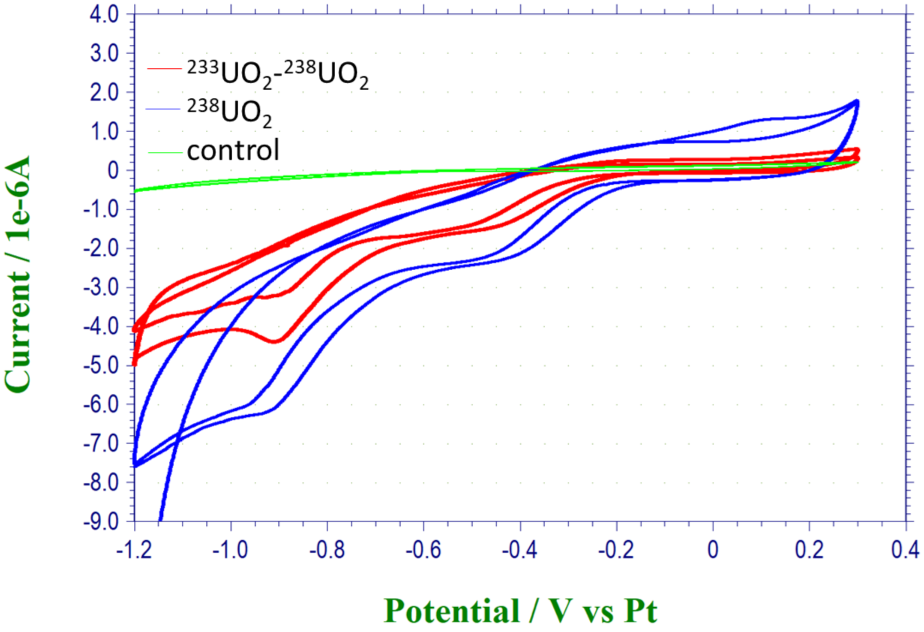

Figure 3.14 CV scans after E_{corr} measurements on $^{233}UO_2$-$^{238}UO_2$ (red), and $^{238}UO_2$ (blue), comparing to control PAMEC without containing UO_2 (green)

To verify whether the E_{corr} measurement is the result from UO_2 electrode, CV scans were performed after the E_{corr} measurements (Figure 3.14). The red cyclic voltammogram records the redox of $^{233}UO_2$-$^{238}UO_2$ electrode after the E_{corr} measurement. It shows the cathodic peak of UO_2 at -0.906 vs Pt, whereas no significant anodic peak in the forward scan. In contrast, there was a noticeable anodic peak observed in the cyclic voltammogram of $^{238}UO_2$ (blue) at 0.098 V vs Pt. The $^{238}UO_2$ was previously exposed to the electrolyte purged with air, its E_{corr} result is shown in Figure 3.12. Purging the electrolyte with air created the oxidizing environment for the $^{238}UO_2$, resulting in a more prominent oxidation peak of UO_2. The cyclic voltammogram of control samples, i.e., PAMEC without UO_2 attached, shows no noticeable redox peaks in the same electrolyte used to test E_{corr} of UO_2.

3.4 X-ray photoelectron Spectroscopy (XPS) analysis of corroded and as-prepared $^{233}UO_2$-$^{238}UO_2$

Three PAMEC devices containing $^{233}UO_2$-$^{238}UO_2$ electrodes were prepared for XPS analyses. PAMEC 1-001 was labelled as-prepared, i.e., without being loaded with electrolyte. Samples 1-002 and 1-003 were loaded with electrolyte purged with N_2 and 4% H_2 for 30 minutes prior to the injection, respectively. The electrolyte was prepared as 0.1M $NaClO_4$ (pH=9.5). The UO_2 samples of 1-002 and 1-003 were exposed to the electrolyte for ~1 hour. The three samples were transferred into a glove box filled with argon that was connected to the load lock of the XPS instrument. Oxygen and moisture levels in the glove box were maintained under 2 ppm. The cells were then disassembled, and the wafers were mounted onto double sided tape for analysis. XPS analysis was performed using an Al-K_α source ($h\upsilon$=1486.7 eV) operating at a chamber base pressure below 2×10^{-9} Torr. High resolution scans were acquired on U 4*f*, C 1*s*, O 1*s*, and Au 4*f* regions at a pass energy of 40 eV. The U 4*f* region was analyzed to understand the near-surface chemical speciation of uranium in the samples. Rather than the absolute binding energy (BE), the BE separation between the satellite and the main peaks were used as the primary indicator for the oxidation states present.

The U 4*f* spectra for the corroded sample exposed to pure N_2 (1-002) presents two features at 381.8 eV and 392.6 eV corresponding to U $4f_{7/2}$ and U $4f_{5/2}$ features respectively (Figure 3.15A). Preliminary curve fitting was carried out on the entire U 4*f* region in accordance with fitting protocols described in Yao et al. [1]. This revealed satellite features at ~3.7 eV and 10 eV above the main peak which are well within those reported for a U(VI) species. The U 4*f* spectra obtained from the sample exposed to H_2 gas (1-003), was found to be almost identical to the one obtained under N_2 exposure (Figure 3.15B). Hence, for both these samples the major uranium species was deduced to be U(VI).

For fitting the as-prepared $^{233}UO_2$-$^{238}UO_2$ sample, we transferred curve fitting parameters corresponding to a U(VI) species, along with using components derived from a well-characterized UO_2 sample as our U(IV) standard. However, only using parameters for U(VI) and U(IV) resulted in a poor fit to experimental spectra. Adding components corresponding to U(V) species, provided a much better fit, resulting in approximately 42% U(VI), 40% U(V), and a minor 18% of U(IV) species in the as-prepared sample (Figure 3.15C).

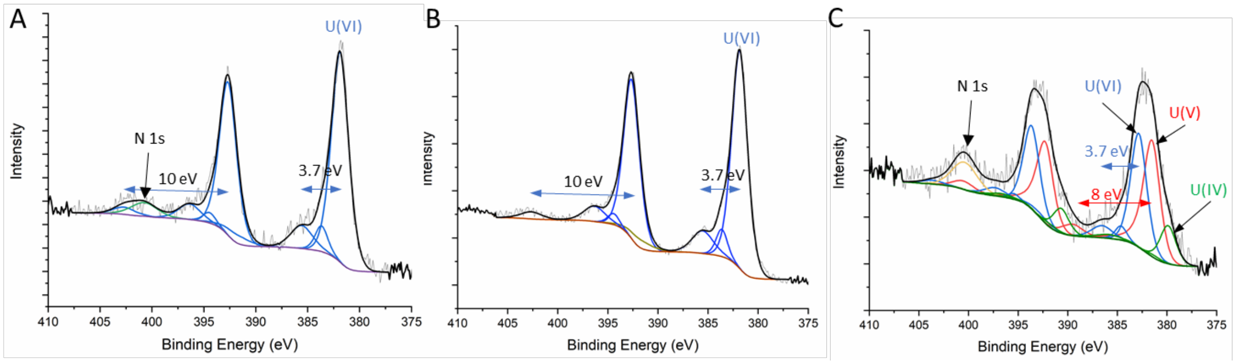

Figure 3.15. U 4f spectral deconvolution for $^{233}UO_2$-$^{238}UO_2$ samples. A) In presence of nitrogen (**1-002**), B) In presence of hydrogen (**1-003**), and C) As-prepared sample (no electrochemistry performed (**I-001**)).

Both the sample exposed to N_2 (I-002) and the one exposed to H_2 (I-003) had oxidized similarly to U(VI) based on XPS. The question to answer is whether the oxidation penetration depth was also the same in both samples. It is also possible that because these were closed systems (i.e., no flow), that the H_2 was consumed too quickly (or escaped) and then radiolytic oxidants enabled U(VI) to form. Even without exposure to an electrolyte, the high specific activity uranium oxide underwent significant oxidation. In Figure 3.16 and Figure 3.17, SEM images from tests I-002 and I-003 are shown. In agreement with the XPS, no obvious differences in the morphology of the particles were observed.

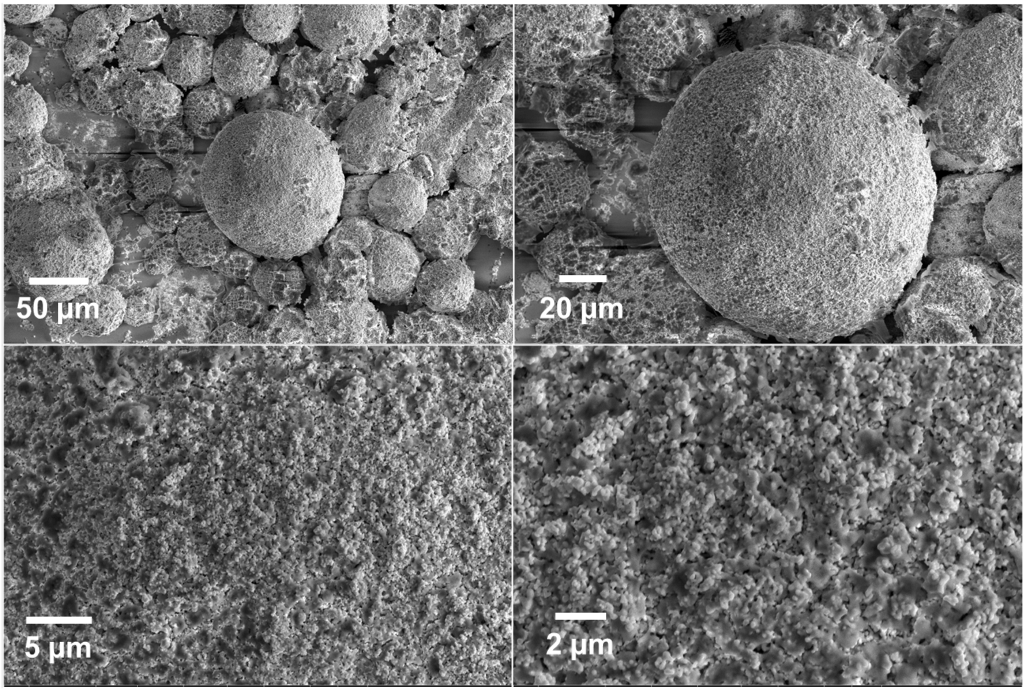

Figure 3.16. SEM images of ^{233}U-doped UO_2 electrode particles from **1-002** test in N_2 only deaerated environment.

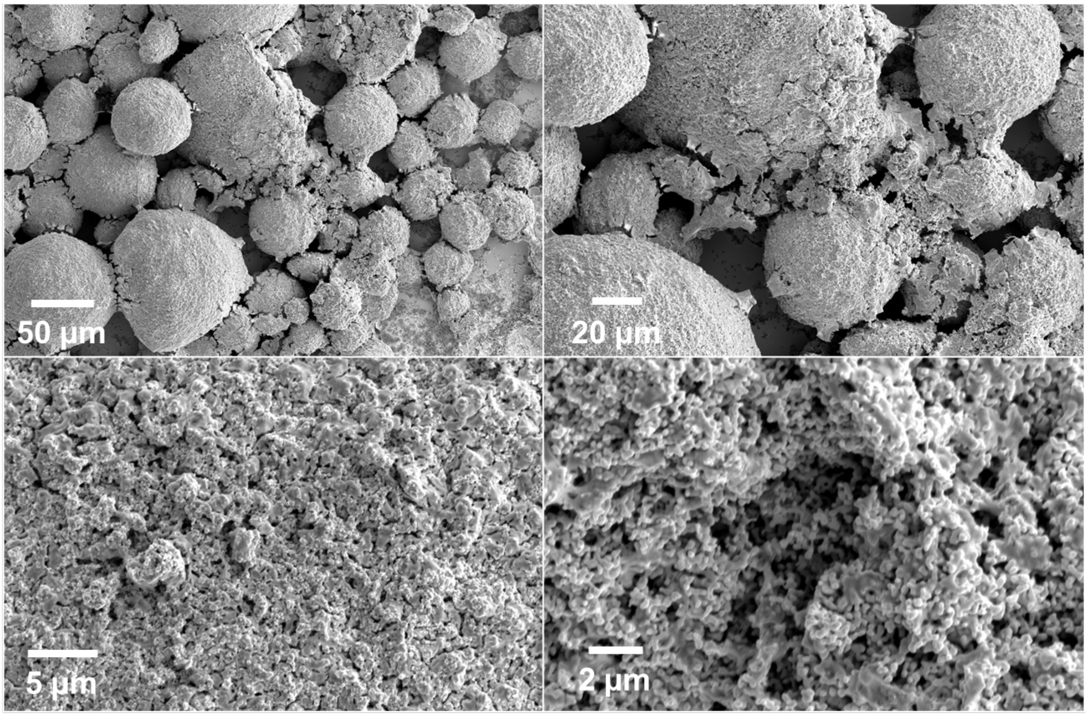

Figure 3.17. SEM images of ^{233}U-doped UO_2 electrode particles from **1-003** test in N_2/H_2 deaerated environment.

4.0 Discussion

The removal pathway for the molecular radiolytic oxidant H_2O_2 is through reactions with e_{aq}^- and •H; in contrast, for H_2 it is the reaction with •OH. Hence, removal of •OH leads to an increase in H_2 concentration. Because β/γ-radiolysis is dominated by radical production, β/γ-fields will tend to destroy H_2. Hence, to correctly model the long-term behavior of SNF, it is important to devise methods that can either reduce the β,γ-field or eliminate it altogether. Consequently, testing of current SNF directly will not yield accurate results the majority of the time with SNF in a repository environment because of the significant β,γ-field from ^{137}Cs and ^{90}Sr. The PAMEC avoids such issues because of the high SA/V of the particles and the small dimensions of the reaction chamber such that β,γ exit the PAMEC before interacting with the solution.

Further, HNO_2/HNO_3 are radiolytically generated from N_2 in aqueous thin films (see Figure 4.1). Note the 20-year FEBEX experiments demonstrate the occurrence of N_2 in the deaerated environment. Indeed, the importance of N_2 and other gases that may also undergo radiolytic effects in the repository environment is unclear and needs to be investigated.

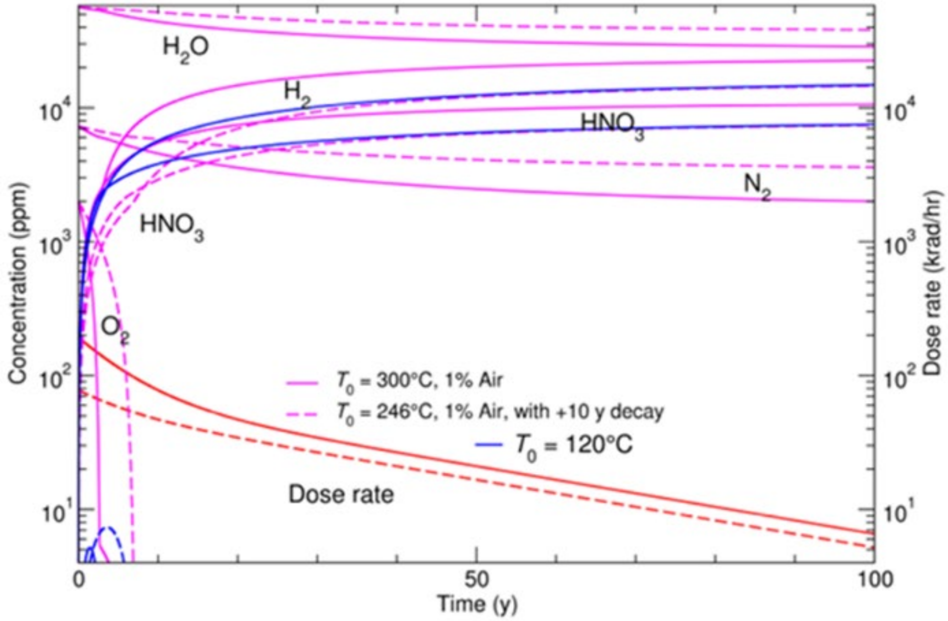

Figure 4.1 Fill Gas Composition over 100 years assuming residual 1 L of water with 1% Air with nominal dose rate (solid line) and with an additional 10-year decay (dashed line) [adapted from [33]].

Although H_2 is generated during radiolysis of water, there is interest in the role that H_2 gas generated from the corrosion of iron under anoxic conditions has on the future corrosion behavior of disposed SNF. A near 20-year test in the FEBEX bentonite site in Switzerland has provide insight into the gaseous environment for an anoxic high level waste repository [34]. The production of H_2, CO_2, N_2, CH_4 and other hydrocarbons was observed, whereas oxygen was consumed within 1.5-2 years (however, note that α-radiolysis yields O_2, as discussed in section 3.3). Interestingly, the N_2 concentration remained at 80-90% throughout. There was no radiation field in these experiments. However, N_2 undergoes radiolytic reactions that can result in generation of HNO_3. Reed and Van Konynenburg [35] developed an equation to describe the yield of HNO_3, in vapor under γ-irradiation, as a function of the gas/liquid ratio and radiolytic conditions:

$$N_t = 2C_0R[1 - \exp(-1.45 \times 10^{-5}\ GD_t)] \tag{4.1}$$

where N_t is the nitrogen fixation (moles/L) at time, t, C_o is the initial concentration of nitrogen in air, R is the air/liquid ratio, G is the G-value for HNO_3 (~1.9), and D is the dose in Mrad/h. Experiments on nuclear waste glass under vapor hydration conditions have demonstrated the effect of HNO_3 on lowering the pH on exposed surfaces [22]. Under γ-irradiation, sufficient HNO_3 was produced to lower the pH and increase the glass dissolution rate.

The clear result from these experiments is that we can eliminate H_2O_2 with H_2 in an α-field. This directly supports the modeling results of Wittman et al. that first proposed this effect [2]. The corrosion rate of the α-doped UO_2 in H_2 matches the corrosion rate of UO_2 (non-doped) in air (see Figure 3.12). Table 3 summarizes the results from the PAMEC experiments. The lowest corrosion potential at -0.158 V was $^{238}UO_2$ with no oxidants present and the high corrosion potential was with ^{233}U-doped UO_2 with N_2 at -0.125 V. The corrosion potential with ^{233}U-doped UO_2 under Ar/H_2 and N_2/H_2, at -0.149 V and -0.135 V, respectively, matched closely with the corrosion potential of $^{238}UO_2$ in air at -0.136 V.

Table 3 Summary of PAMEC Electrochemical Results

Testing No.	Electrode	Gas Introduced Sequentially	Ecorr vs Pt (V)*	Figure No.
1	$^{233}UO_2$-$^{238}UO_2$	N_2, 4% H_2 in N_2, N_2	-0.125 (N_2), -0.135 (H_2), -0.135 (N_2)	Figure 3.11 E_{corr} comparison between $^{233}UO_2$-$^{238}UO_2$ (red curve) and $^{238}UO_2$ (blue curve) electrodes shows different responses to dissolved H_2 in solution.
2	$^{238}UO_2$	N_2, 4% H_2 in N_2	-0.158 (N_2), -0.152(H_2)	
3	$^{233}UO_2$-$^{238}UO_2$	Ar, 2.7% H_2 in Ar	-0.138 (Ar), -0.149 (H_2)	Figure 3.12 E_{corr} of (A) $^{233}UO_2$-$^{238}UO_2$ electrode and (B) $^{238}UO_2$ electrode exposed in the electrolyte purged with different gases.
4	$^{238}UO_2$	Ar, dry air	-0.136 (Ar), -0.135 (H_2)	

* The potential value is taken from the data point right before switching the gas or end of measurement.

The PAMEC is an adaptable tool that will enable determination of the changes in radiation field, gas components, including dissolved CO_2 and N_2, as well as solid phase interactions, and the impact these have on the E_{corr} of UO_2.

Radiolytic effects are not currently included in the FMD process model as developed by Jerden et al. [5]. However, this report has demonstrated that the results are physically accurate and predictable for α-radiolysis, and it would be beneficial for PA calculations to include them in any future model. Finally, if the current FMD process model is used as part of PA or as a training data set for more advanced models, without including detailed radiation chemistry, it cannot accurately represent the behavior of SNF in an anoxic geologic repository.

5.0 References

[1] J. Yao, N. Lahiri, S. Tripathi *et al.*, “A microfluidic electrochemical cell for studying the corrosion of uranium dioxide (UO2),” *RSC Advances,* vol. 12, no. 30, pp. 19350-19358, 2022.

[2] R. S. Wittman, E. C. Buck, E. J. Mausolf *et al.*, “Conditions for critical effects in the mass action kinetics equations for water radiolysis,” *The Journal of Physical Chemistry A,* vol. 118, no. 51, pp. 12105-12110, 2014.

[3] L. Liu, and I. Neretnieks, “The Effect of Hydrogen on Oxidative Dissolution of Spent Fuel,” *Nuclear Technology,* vol. 138, no. 1, pp. 69-78, 2002/04/01, 2002.

[4] D. W. Shoesmith, “Fuel corrosion processes under waste disposal conditions,” *Journal of Nuclear Materials,* vol. 282, no. 1, pp. 1-31, 11//, 2000.

[5] J. L. Jerden, K. Frey, and W. Ebert, “A multiphase interfacial model for the dissolution of spent nuclear fuel,” *Journal of Nuclear Materials,* vol. 462, pp. 135-146, 2015/07/01/, 2015.

[6] P. E. Mariner, T. M. Berg, K. W. Chang *et al.*, *Surrogate Model Development of Spent Fuel Degradation for Repository Performance Assessment*, United States, 2020.

[7] M. E. Broczkowski, J. J. Noël, and D. W. Shoesmith, “The inhibiting effects of hydrogen on the corrosion of uranium dioxide under nuclear waste disposal conditions,” *Journal of Nuclear Materials,* vol. 346, no. 1, pp. 16-23, 11/1/, 2005.

[8] J. Bruno, and K. Spahiu, “The long-term effect of hydrogen on the UO2 spent fuel stability under anoxic conditions: Findings from the Cigar Lake Natural Analogue study,” *Applied Geochemistry,* vol. 49, pp. 178-183, 10//, 2014.

[9] P. Carbol, P. Fors, T. Gouder *et al.*, “Hydrogen suppresses UO2 corrosion,” *Geochimica et Cosmochimica Acta,* vol. 73, no. 15, pp. 4366-4375, 8/1/, 2009.

[10] K. Ollila, E. Myllykylä, M. Tanhua-Tyrkkö *et al.*, “Dissolution rate of alpha-doped UO2 in natural groundwater,” *Journal of Nuclear Materials,* vol. 442, no. 1, pp. 320-325, 2013/11/01/, 2013.

[11] B. Pastina, and J. A. LaVerne, “Effect of Molecular Hydrogen on Hydrogen Peroxide in Water Radiolysis,” *The Journal of Physical Chemistry A,* vol. 105, no. 40, pp. 9316-9322, 2001/10/01, 2001.

[12] E. C. Buck, R. S. Wittman, F. N. Skomurski *et al.*, *Radiolysis Process Model*, United States, 2012.

[13] B. D. Hanson, *The burnup dependence of light water reactor spent fuel oxidation,* PNNL-11929; R&D Project: 26570; Other: ON: DE98058013; BR: N/A; TRN: 99:002115 United States 10.2172/291169 R&D Project: 26570; Other: ON: DE98058013; BR: N/A; TRN: 99:002115 INIS; OSTI as DE98058013 PNNL English, ; Pacific Northwest National Lab., Richland, WA (United States), 1998.

[14] E. C. Buck, E. J. Mausolf, B. K. McNamara *et al.*, “Nanostructure of metallic particles in light water reactor used nuclear fuel,” *Journal of Nuclear Materials,* vol. 461, pp. 236-243, 2015.

[15] R. A. Clark, M. A. Conroy, T. G. Lach *et al.*, “Distribution of metallic fission-product particles in the cladding liner of spent nuclear fuel,” *npj Materials Degradation,* vol. 4, no. 1, pp. 4, 2020/01/30, 2020.

[16] S. H. Kessler, T. G. Lach, K. E. Garrett *et al.*, “Direct observations of Pd–Te compound formation within noble metal inclusions in spent nuclear fuel,” *Journal of Nuclear Materials,* vol. 538, pp. 152249, 2020/09/01/, 2020.

[17] E. C. Buck, and R. S. Wittman, *Radiolysis Model Formulation for Integration with the Mixed Potential Model,* PNNL-23459; Other: AF5865010 United States

10.2172/1168932 Other: AF5865010 PNNL English, ; Pacific Northwest National Lab. (PNNL), Richland, WA (United States), 2014.

[18] A. J. Elliot, and D. R. McCracken, “Computer modelling of the radiolysis in an aqueous lithium salt blanket: Suppression of radiolysis by addition of hydrogen,” *Fusion Engineering and Design,* vol. 13, no. 1, pp. 21-27, 1990/08/01/, 1990.

[19] E. C. Buck, and R. S. Wittman, *Radiolysis Model Formulation for Integration with the Mixed Potential Model*, United States, 2014.

[20] E. C. Buck, and J. K. Bates, “Microanalysis of colloids and suspended particles from nuclear waste glass alteration,” *Applied Geochemistry,* vol. 14, no. 5, pp. 635-653, 1999.

[21] E. C. Buck, and R. S. Wittman, *Addition of Bromide to Radiolysis Model Formulation for Integration with the Mixed Potential Model,* PNNL-25539 United States 10.2172/1592703 PNNL English, ; Pacific Northwest National Lab. (PNNL), Richland, WA (United States), 2016.

[22] D. J. Wronkiewicz, J. K. Bates, E. C. Buck *et al.*, *Radiation effects in moist-air systems and the influence of radiolytic product formation on nuclear waste glass corrosion*, United States, 1997.

[23] E. C. Buck, E. J. Mausolf, B. K. McNamara *et al.*, “Sequestration of radioactive iodine in silver-palladium phases in commercial spent nuclear fuel,” *Journal of Nuclear Materials,* vol. 482, pp. 229-235, Dec 15, 2016.

[24] D. Sassani, J. Birkholzer, R. Camphouse *et al.*, *SFWST Disposal Research R&D 5-Year Plan - FY2021 Update*, United States, 2021.

[25] X.-Y. Yu, J. Yao, E. C. Buck *et al.*, “In situ liquid SIMS analysis of uranium oxide,” *Surface and Interface Analysis,* vol. 52, no. 7, pp. 454-459, 2020.

[26] A. J. Popel, S. R. Spurgeon, B. Matthews *et al.*, “An Atomic-Scale Understanding of UO2 Surface Evolution during Anoxic Dissolution,” *ACS Applied Materials & Interfaces,* vol. 12, no. 35, pp. 39781-39786, 2020/09/02, 2020.

[27] R. C. Ewing, “Long-term storage of spent nuclear fuel,” *Nat Mater,* vol. 14, no. 3, pp. 252-257, 03//print, 2015.

[28] E. C. Buck, D. J. Wronkiewicz, P. A. Finn *et al.*, “A new uranyl oxide hydrate phase derived from spent fuel alteration,” *Journal of Nuclear Materials,* vol. 249, no. 1, pp. 70-76, 9/2/, 1997.

[29] R. J. Finch, and R. C. Ewing, “The corrosion of uraninite under oxidizing conditions,” *Journal of Nuclear Materials,* vol. 190, pp. 133-156, 1992/08/02/, 1992.

[30] E. C. Buck, P. A. Finn, and J. K. Bates, “Electron energy-loss spectroscopy of anomalous plutonium behavior in nuclear waste materials,” *Micron,* vol. 35, no. 4, pp. 235-243, 2004/06/01/, 2004.

[31] Y. Peled, E. Krent, N. Tal *et al.*, “Electrochemical Determination of Low Levels of Uranyl by a Vibrating Gold Microelectrode,” *Analytical Chemistry,* vol. 87, no. 1, pp. 768-776, 2015/01/06, 2015.

[32] D. W. Shoesmith, W. H. Hocking, S. Sunder *et al.*, “Electrochemical studies of SIMFUELS,” *Journal of Alloys and Compounds,* vol. 213-214, pp. 551-553, 1994/10/01/, 1994.

[33] R. S. Wittman, *Radiolysis Model Sensitivity Analysis for a Used Fuel Storage Canister*, United States, 2013.

[34] J. Hadi, P. Wersin, V. Serneels *et al.*, “Eighteen years of steel–bentonite interaction in the FEBEX in situ test at the Grimsel Test Site in Switzerland,” *Clays and Clay Minerals,* vol. 67, no. 2, pp. 111-131, 2019/04/01, 2019.

[35] D. T. Reed, and R. A. Van Konynenburg, "Effect of Ionizing Radiation on Moist Air Systems." p. 393.

[36] T. Vitova, I. Pidchenko, D. Fellhauer *et al.*, “The role of the 5f valence orbitals of early actinides in chemical bonding,” *Nature Communications,* vol. 8, no. 1, pp. 16053, 2017/07/06, 2017.

[37] G. Kauric, O. Walter, A. Beck *et al.*, “Synthesis and characterization of nanocrystalline U1-xPuxO2(+y) mixed oxides,” *Materials Today Advances,* vol. 8, pp. 100105, 2020/12/01/, 2020.

Appendix A

A.1 X-ray Absorption Experiments: Collaboration with Karlsruhe Institute of Technology (KIT)

Our collaboration with a research group at the Karlsruhe Institute of Technology (KIT) in Germany is ongoing. We have built an electrical feed-through that can be accommodated in their glove box for performing in situ and in operando analysis, using the PAMEC technique, and their high-energy resolution x-ray absorption near edge structure (HR XANES) spectroscopy technique.

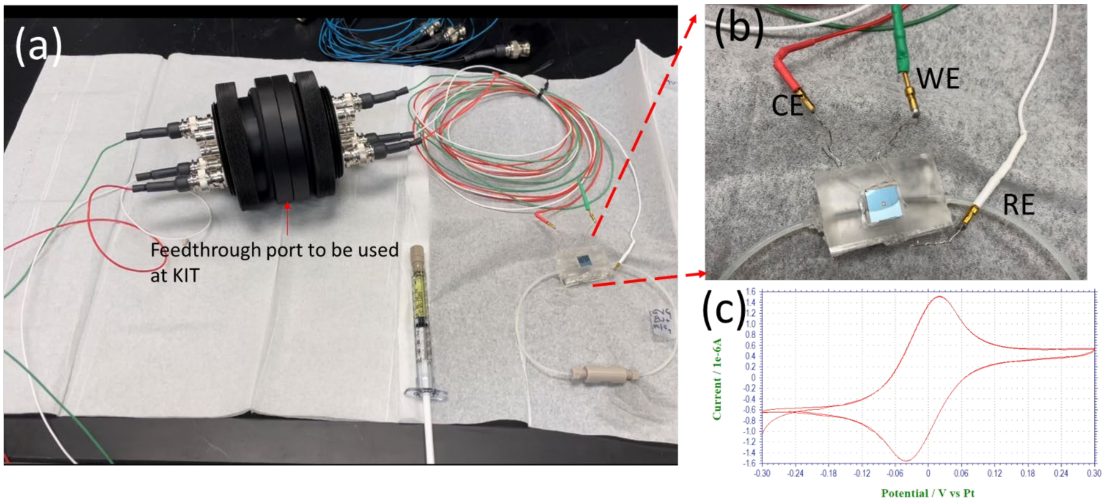

Figure A.1 (a) Electrical feed-through connection testing, with (b) closer look at the connection of three-electrode PAMEC, and (c) cyclic voltammogram of ferro/ferri redox couple at 10 mV/s vs Pt reference electrode.

In addition, the collaboration with KIT is ongoing. The electrical feed-through was installed with BNC connectors and cables. The connection testing using PAMEC control device loaded with 2 mM $K_4Fe(CN)_6$ and 2 mM $K_3Fe(CN)_6$ in 0.1 M aqueous KCl is shown in Figure A.1. HR XANES provides a high energy resolution and thus yields the possibility to distinguish a minor contribution of one actinide oxidation state in mixtures [36]. Especially for U(IV) and U(V) in a UO_2 structure, large shifts in edge positions could be seen in their paper [37], which provides the possibility to differentiate minor contributions of U(V). With the application of PAME, and KIT's beamline, we are hoping to address the questions as below:

1. How will the U oxidation state change over the course of an electrochemical oxidation?

2. During the corrosion experiments, how does the oxidation state and local environment of U develop?

Pacific Northwest
National Laboratory

902 Battelle Boulevard
P.O. Box 999
Richland, WA 99354

1-888-375-PNNL (7665)

www.pnnl.gov